Journal Pre-proofs

Dynamic analysis and structure optimization on trapezoidal wave generator for eliminating the over deviation of the residual wave in shock test measurement

Jingjing Wen, Houpu Yao, Bin Wu, Ze Ji, Lihua Wen, Man Xu, Yi Jin, Xunliang Yan

Please cite this article as: J. Wen, H. Yao, B. Wu, Z. Ji, L. Wen, M. Xu, Y. Jin, X. Yan, Dynamic analysis and structure optimization on trapezoidal wave generator for eliminating the over deviation of the residual wave in shock test measurement, *Measurement* (2021), doi: https://doi.org/10.1016/j.measurement.2021.109665

Dynamic analysis and structure optimization on trapezoidal wave generator for eliminating the over deviation of the residual wave in shock test measurement

Jingjing Wen[a,d,*], Houpu Yao[b], Bin Wu[a], Ze Ji[c], Lihua Wen[a,*], Man Xu[d], Yi Jin[d], Xunliang Yan[a,*]

[a.] School of Astronautics, Northwestern Polytechnical University, Xi'an, Shaanxi 710072, China;

[b.] JD Finance America Corporation, Mountain View, CA 94043, USA;

[c.] School of Engineering, Cardiff University, Cardiff CF243AA, UK;

[d.] Suzhou Dongling Vibration Test Instrument Co., Ltd., Suzhou, Jiangsu 215163, China;

[*.] Correspondence: Lhwen@nwpu.edu.cn (L. Wen); xly_nwpu@126.com (X. Yan); wjj1990@mail.nwpu.edu.cn (J. Wen).

Abstract: In this work, a new separate-style trapezoidal wave generator (TWG) is designed to alleviate the over deviation of residual waves in trapezoidal shock waveform generation processes. Firstly, a hypothesis is proposed that this over deviation is caused by the impact between the piston and the end cover of the TWG by analyzing the dynamic behavior of the TWG during shock tests, and, subsequently, verified with finite element simulation. Then, a dynamic model is established to describe the impact behavior between the piston and the end cover based on the 1D continuous rod theory. Several parameters, including the impact velocity, the attached mass, the piston weight, the stiffness of the inner cushion, the piston rod length, and the piston rod diameter, are analyzed to estimate this impact behavior. Lastly, the separate-style TWG is designed by implementing a simple and effective modification on the traditional TWG in accordance with the parameters' analysis.

Key words: shock test measurement; trapezoidal wave generator; over deviation of residual wave; 1D continuous rod; structure optimization

1. Introduction

Consumer electronic products, such as mobile phones, laptop computers, audio players, and tablet PCs, have become personal necessities used daily. These products would undergo a variety of shock environments, such as collision with other objects during storage, shock loads derived by transport jolting, and accidental drops on the ground, during the usable lifetime, which would damage these products [1], [2]. To verify if the electronic products could withstand such drop impacts and improve the reliability of the electronic products, many stringent drop test standards are imposed on the electronic products, and passing the requirements of these standards is a mandatory step before launching the products into the market [3], [4]. The representative standards include JESD22-B110/JESD22-B111, IEC-68-2-29, EIA-364-27, etc., which were published by several standardization bodies, such as Joint Electron Device Engineering Council (JEDEC), International Electrotechnical Commission (IEC), and Electronic Industries Alliance (EIA) [5]-[7]. With these standards, there are three mainstream methods to simulate the impact environment, namely acceleration-time pulse-based simulation method [8], [9], shock response spectrum-based simulation method [10], [11], and finite element method (FEM) simulation [12], [13]. Among them, the acceleration-time pulse-based simulation method has been being widely applied for the shock test of various electronic products in industry, of which the waveforms of the specified acceleration-time pulses, as shown in Fig. 1, mainly include half-sine waveform, trapezoidal waveform, and final-peak sawtooth waveform [14], [15]. Among them, the trapezoidal shock pulse can produce a higher response over a wider spectrum than both the half-sine and the final-peak sawtooth shock pulses, and is widely used as the shock test waveform to estimate the reliability of electronic products [16].

Nomenclature

|			
F_e	elastic force of the rubber cushion	F_p	gas pressure of the TWG
M_s	mass sum of the TWG and the drop shock tester's table	x_2	deformation of the rubber cushion
K_2	stiffness of the rubber cushion	x_1	absolute displacement of the drop shock tester's table toward the base
K_1	nonlinear stiffness of the TWG	K_e	equivalent stiffness of K_1 and K_2 in series
F_{p0}	initial gas pressure of the TWG	τ_1	duration of the rising and descending ramp
τ_2	duration of the constant-acceleration phase	P_h	pulse height of the trapezoidal waveform
ω_2	natural frequency of the rubber cushion	v_0	initial velocity of drop shock tester's table
h	drop height of the TWG	$\boldsymbol{M}^e$	mass matrix of the FEM model
$\boldsymbol{C}^e$	damping matrix of the FEM model	$\boldsymbol{K}^e$	stiffness matrix of the FEM model
$\ddot{\boldsymbol{x}}^e$	acceleration vector of the FEM model	$\dot{\boldsymbol{x}}^e$	velocity vector of the FEM model
$\boldsymbol{x}^e$	displacement vector of the FEM model	$\boldsymbol{Q}$	external force vector of the FEM model
Δt	computing time step of the FEM model	$\boldsymbol{x}^e_{t+\Delta t}$	displacement vector at time $t+\Delta t$
$\boldsymbol{x}^e_t$	displacement vector at time t	$\boldsymbol{x}^e_{t-\Delta t}$	displacement vector at time t-Δt
$\boldsymbol{Q}_t$	external force vector at time t	Δt_{stable}	time step in the dynamic explicit solver
L^e_{min}	minimum mesh size of the FEM model	C_d	material wave velocity
E_M	elastic modulus of the material assigned to the FEM model	ρ_M	density of the material assigned to the FEM model
l	length of the piston shaft	A	cross-section area of the piston shaft
ρ	density of the piston shaft	E	modulus of elasticity of the piston shaft
m	mass of the piston	M	mass of the impact hammer
k	stiffness of the equivalent spring	$u(x, t)$	longitudinal vibration displacement of the rod (piston shaft) at time t
c	specific stiffness of the rod	v	initial velocity of the piston
ζ	non-dimensional parameter, $\zeta = \frac{x}{l}$	τ	non-dimensional parameter, $\tau = \frac{ct}{l}$
$\tilde{k}$	non-dimensional parameter, $\tilde{k} = \frac{kl}{EA}$	α	non-dimensional parameter, $\alpha = \frac{\rho Al}{M}$
η	non-dimensional parameter, $\eta = \frac{m}{\rho Al}$	$\tilde{u}(\zeta, \tau)$	non-dimensional parameter, $\tilde{u}(\zeta, \tau) = \frac{cu(x, t)}{vl}$
$U(\zeta)$, $T(\tau)$	separation of variables, $\tilde{u}(\zeta, \tau) = U(\zeta)T(\tau)$	λ	non-dimensional natural frequency
λ_i	i-th non-dimensional natural frequency	$\tilde{A}$, $\tilde{B}$	amplitudes of the principal modes
$\tilde{C}_i$, $\tilde{D}_i$	amplitudes of the i-th time function	$U_i(\zeta)$, $U_j(\zeta)$	principal mode with the non-dimensional natural frequency λ_i and λ_j respectively
$\delta(\cdot)$	Dirac delta function	F	impact force
T_F	impact duration	d	diameter of the piston shaft
l_I	thickness of the inner cushion	E_I	elastic modulus of the inner cushion
υ	Poisson's ratio of the inner cushion	n_I	number of the inner cushions
A_I	effective contact area of the inner cushion	$\varepsilon_r, \varepsilon_\theta, \varepsilon_z$	strain of the inner cushion in the radial, tangential, and axial directions respectively
$\sigma_r, \sigma_\theta, \sigma_z$	stress of the inner cushion in the radial, tangential, and axial directions respectively	$[L_i, U_i]$	search range for the i-th non-dimensional natural frequency
$\tilde{F}$	non-dimensional parameter, $\tilde{F} = \frac{FC}{EAv}$		
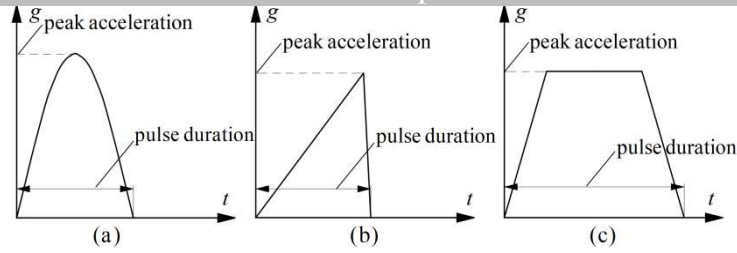
Fig. 1. Specified acceleration-time waveforms used to model actual shock environment. Shown in the figure are (a) half-sine waveform, (b) final-peak sawtooth waveform, and (c) trapezoidal waveform.

In order to generate a satisfactory shock waveform, various waveform generators, as the crucial component in the shock test system, are developed by engineers and researchers. In summary, as shown in Fig. 2, the rubber waveform generators is extensively used to generate half-sine shock pulses [8]; the lead cone is widely applied to produce final peak sawtooth shock pulses [17]; and the pneumatic cylinder-type TWG is usually employed to generate trapezoidal shock pulses [18].

Fig. 2. Various types of waveform generators. Shown in the figure are (a) the rubber waveform generator, (b) the lead cone, and (c) the pneumatic cylinder-type TWG.

However, due to the strict waveform requirements in shock tests [5]-[7] and the complex structure design of the cylinder-type TWG, it is usually not easy in practice to generate a satisfactory trapezoidal shock waveform [19]. To the authors' best knowledge, there is still a lack of effective research on the working principle of TWG, which would usually involve large time- and resource- cost when designing or adjusting TWG. Many of the previous works in this field are concentrated on the structural reliability of electronic components under trapezoidal shock pulses [20]-[22]. Additionally, Neuburg investigates the shock response spectrum of trapezoidal shock waveforms and analyzes the reliability of driving disk under trapezoidal shock pulses [19]. Parzianello et al. develops an effective method to estimate shock response spectrum propagating in plates excited by trapezoidal shock pulse [23]. Jin et al. proposes a piecewise linear dynamic model to describe the working principle of TWG by abstracting the TWG as a pre-pressured linear spring [24]. The pulse amplitude and the pulse duration, which are two key parameters in the acceleration-time pulse-based shock test [25], can be predicted based on this piecewise linear dynamic model. However, the effect of the residual wave on the quality of the overall trapezoidal waveform is not considered. In practice, the authors find that the over deviation of the residual wave often occurs in practical trapezoidal wave shock tests, which will give rise to the shock test failure directly. As examples presented in Fig. 3, the residual waves of the trapezoidal shock pulses are both out of the tolerance, and, hence, these generated trapezoidal waveforms cannot meet the requirements of the shock test specification, although the pulse amplitudes and the pulse durations are all satisfying desired characteristics. In allusion to this problem, it is necessary to investigate the occurrence mechanism of the over deviation phenomenon and further propose modification measures to alleviate or suppress this phenomenon.
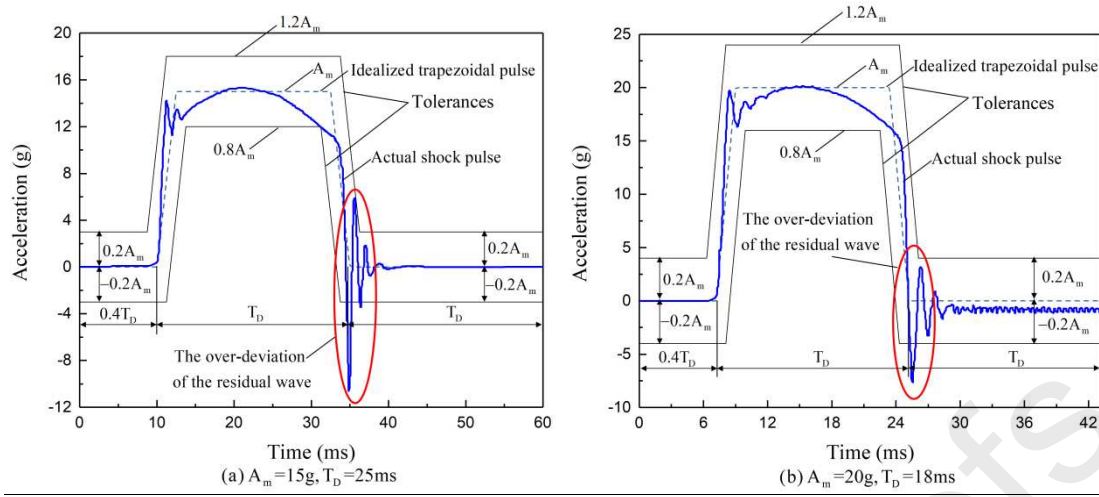
Fig. 3. Two typical cases of failed shock test posed by the over deviation of the residual wave. These two typical examples are attained from our practical experiments. The specification shown in the figure is based on IEC 60068-2-27-2008 [6], where A_m and T_D represent the pulse amplitude and the pulse duration of the specified idealized trapezoidal shock pulse respectively.

In this work, the dynamics behavior during the shock test of a TWG is firstly analyzed qualitatively. Based on this analysis, a hypothesis is proposed that the over deviation of the residual wave is caused by the impact between the piston and the end cover of the TWG at the stroke terminal of the shock test. Subsequently, a FEM model of a TWG is constructed to simulate the collision of the piston against the end cover. The simulated result shows that the calculated residual wave has a similar oscillation trend with the experimental result, which verifies the proposed hypothesis indirectly. Then, accordingly, the longitudinal impact between the piston and the end cover is simplified as a 1D continuous rod model, and the impact force-time curves are calculated with mode superposition method. Meanwhile, the effect of the structural parameters of the TWG on the impact behavior between the piston and the end cover can be analyzed based on the established 1D continuous rod model. The analyzed parameters include the impact velocity, the attached mass, the piston weight, the equivalent stiffness of the inner cushion, the length of the piston rod, and the diameter of the piston rod. In guidance of the analysis on these parameters, several structural modifications are proposed and designed on the TWG. The experimental shock test results show that these structural modifications are implementable and can suppress the over deviation of the residual wave effectively. The modified TWG can be used to generate satisfactory trapezoidal shock waveforms in shock tests. The main insights and contributions of this work are highlighted below:

(1) Through dynamic analysis and FEM simulation, the over deviation of residual waves is diagnosed and verified to be caused by the impact of the piston to the end cover of the TWG at the stroke terminal of the shock test.

(2) Based on the mechanism analysis of the over deviation of the residual wave, a longitudinal 1D continuous rod model is established to describe the dynamic behavior of the impact between the piston and the end cover, and the structural parameters of TWG can be optimized to reduce the impact magnitude between the piston and the end cover. The calculation results through this model can be used to guide the optimal design for the TWG.

(3) Several modifications are proposed according to the analytical study on the changes in the structural parameters, and the practical tests show that these modifications can alleviate the over deviation problem of the residual wave in trapezoidal waveform shock tests effectively. Meanwhile, the modified TWG can be used to generate satisfactory trapezoidal shock waveforms.

2. The dynamics modeling of the TWG
2.1 The mechanical structure and the working principle of the TWG
As shown in Fig. 1(b), an idealized trapezoidal shock waveform consists of three parts: the

4

constant-acceleration portion and the symmetrical rising and descending ramps. Owing to the existence of the constant-acceleration portion, the trapezoidal shock waveform should be produced by generators with nonlinear elasticity. At present, the trapezoidal shock waveform is mainly generated by combining the pneumatic cylinder-type TWG and a drop shock tester cooperatively. The mechanical structure of the pneumatic cylinder-type TWG is diagramed in Fig. 4, of which the constant pressure gas in the sealed chamber is used to produce the constant-acceleration value in the middle of the waveform.
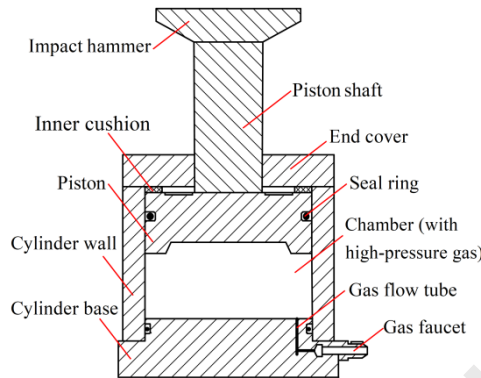

Fig. 4. The schematic of the mechanical structure of the pneumatic cylinder-type TWG.

As shown in Fig. 5, the installation methods between the drop shock tester and the TWG can be divided into two types: vertical installation and inverted installation. It can be found that, with the inverted installation, the TWG is fixed together with the shock tester's table, while, with the vertical installation, the TWG is mounted on the shock tester's base. The working procedures of these two installation types are analogous: firstly, raise the table along the guide rods to a desired height; then, free-fall the table so that the TWG can be impacted with a desired initial velocity; lastly, the acceleration-time signal can be measured with the accelerometer mounted on the shock tester's table. The details of the working principles of the drop shock tester can be referred to in [26].
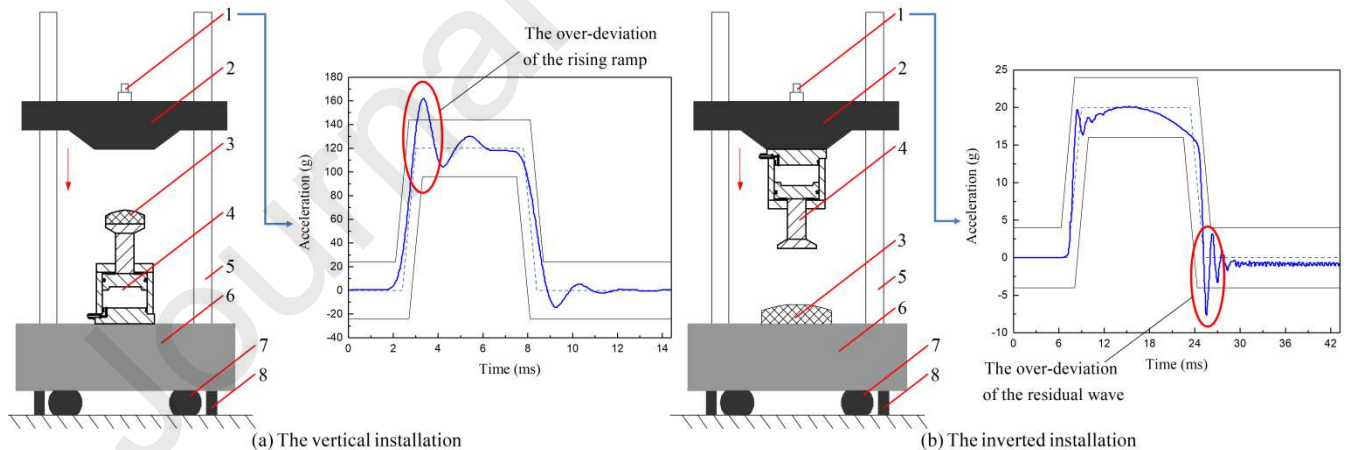
Fig. 5. Two installation styles between the drop shock tester and the TWG. The main components indexed in this figure include 1-accelerometer, 2-table of the drop shock tester, 3-rubber cushion, 4-TWG, 5-drop guide rods, 6-base of the drop shock tester, 7-bellows-type air springs, and 8-dampers of the drop shock tester.

On the other hand, it can be observed from Fig. 5 that both the trends and the magnitudes of the shock waveforms generated from these two installation styles are quite different. In the vertical installation style, the impact force will be directly transmitted to the table through the impact hammer at the moment of collision between the table and the TWG, resulting in the out of tolerance at the rising ramp of the generated shock waveform. In the

case of the inverted installation, the impact force will be transmitted to the table through the high-pressure gas in the chamber of the TWG, which suppress the over deviation of the rising ramp to a certain extent. Therefore, the inverted installation is adopted more widely in practical shock tests than the vertical installation style, though the out of tolerance still exists in the residual wave. Also, this work mainly focuses on the investigation of the inverted installation approach.

2.2 Dynamic analysis for the TWG

As shown in Fig. 6(a), when the table and the TWG are together in free fall motion, the pressure in the TWG is an internal force, such that the acceleration of the table is zero (neglecting the gravity). Then, as shown in Fig. 6(b), when the impact hammer of the TWG hits the rubber cushion, the rubber cushion will be compressed by the TWG, and the resulting elastic force F_e will increase with the incremental compression of the rubber cushion. This process results in the rising ramp of the trapezoidal waveform presented in Fig. 6(d). Where after, with the further compression of the rubber cushion, F_e will be greater than the gas pressure of the TWG (denoted as F_p), and, thus, the piston will move upward towards the cylinder base of the TWG. Subsequently, with the upward movement of the piston, the gas in the TWG will be further compressed, and, accordingly, $F_p > F_e$, leading to the downward movement of the piston. As depicted in Fig. 6(d), this process brings the constant-acceleration portion of the trapezoidal waveform. Note that, owing to the upward and downward motion of the piston, the acceleration between the rising ramp and the descending ramp is approximated as an elliptic curve, but this elliptic curve still can be contained in the tolerance range if the chamber volume and the initial gas pressure of the TWG is properly designed. Lastly, with the downward movement of the piston, F_p returns to the initial pressure, and, correspondingly, the deformation of the rubber cushion will be restored, i.e., the impact hammer will be separated from the rubber cushion, and F_e returns to its initial value. This process gives rise to the descending ramp in the trapezoidal waveform. However, as shown in Fig. 6(c), during the separation between the impact hammer and the rubber cushion, there is still a relative velocity between the piston and the end cover of the TWG, which will pose the impact between these two components. The authors consider that the impact between the piston and the end cover is the cause of the unexpected oscillations at the end of the descending ramp.
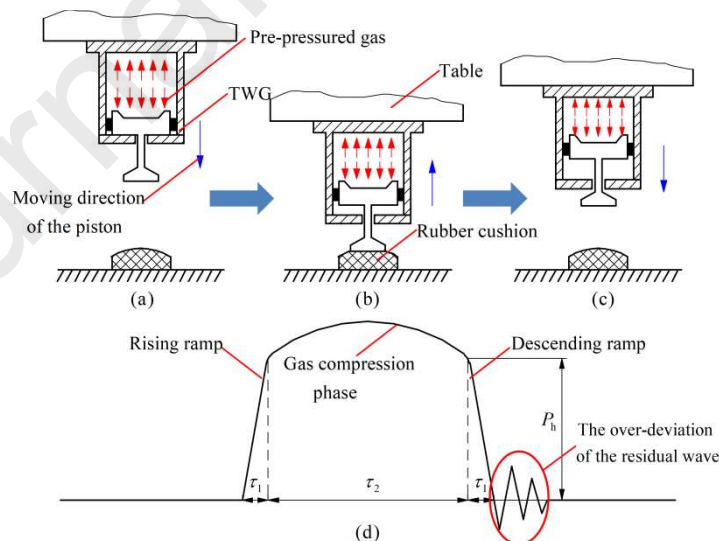

Fig. 6. The schematic diagram for the dynamic analysis of the TWG. For more details about simulating the flow patterns of the gas in the TWG, we encourage readers to refer to [27].

As illustrated in Fig. 7, a piecewise linear spring-mass model of TWG in [24] describes the dynamics behavior of the TWG during shock tests clearly, which can be expressed as follows:

$$\begin{cases} M_s\ddot{x}_2 + K_2x_2 = 0, & |x_2| \le F_{p0}/K_2 \\ M_s\ddot{x}_1 + K_ex_1 = 0, & |x_2| > F_{p0}/K_2. \end{cases} \tag{1}$$

In Fig. 7 and Eq.(1), M_s is the mass sum of the TWG and the drop shock tester's table; x_2 is deformation of the rubber cushion; K_2 is the stiffness of the rubber cushion; x_1 is the absolute displacement of the drop shock tester's table toward the base; K_1 is the nonlinear stiffness of the TWG; $K_e = K_1K_2/(K_1+K_2)$ is the equivalent stiffness of K_1 and K_2 in series; and F_{p0} is the initial gas pressure of the TWG. According to this model, as shown in Fig. 6(d), the pulse duration of a trapezoidal waveform is equivalent to $2\tau_1+\tau_2$, where τ_1 is the duration of the rising and descending ramp, and τ_2 is the duration of the constant-acceleration phase. P_h is the pulse height of the trapezoidal waveform. τ_1, τ_2 and P_h can be calculated as follows:

$$\begin{cases} \tau_1 = \frac{1}{\omega_2}\arcsin\left(\frac{\omega_2 x_2}{v_0}\right) \\ \tau_2 = \frac{2}{\omega_2}\sqrt{\frac{2M_sgK_2h}{F_{p0}^2} - 1}, \\ P_h = \omega_2^2 x_2 \end{cases} \tag{2}$$

where $\omega_2 = \sqrt{K_2/M_s}$ is the natural frequency of the rubber cushion and $v_0 = \sqrt{2gh}$ is the initial velocity of the table (h is the drop height of the TWG). It can be found from Eq.(2) that the pulse duration and the pulse amplitude are determined by the stiffness of the rubber cushion, the mass sum of the table and the TWG, the drop height of the TWG, and the initial gas pressure.
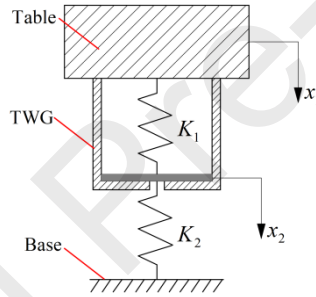
Fig. 7. The piecewise nonlinear dynamics model of the TWG.

2.3 FEM analysis for simulating the shock test process of the TWG

With the aim to further verify the hypothesis that the over deviation of the residual wave is caused by the impact between the piston and the end cover, as shown in Fig. 8(a), an FEM model is established with linear mesh in ABAQUS software to simulate the dynamic behavior of the TWG during shock tests. Without loss of generality, a trapezoidal shock waveform with 15 g-18 ms is employed as a study-case to implement the comparison between the experimental shock waveform and the FEM-simulation result.

As shown in Fig. 8(a), the FEM model mainly includes six parts: the table, the TWG package, the piston, the piston shaft, the impact hammer, and the inner cushion. The material assignments and mesh characteristics of this FEM model are listed in Table 1. In this FEM model, the Mooney-Rivlin model is adopted to describe the hyper-elasticity of the inner cushion, and the Rivlin coefficients are set as C_{10}=0.47 MPa, C_{01}=0.14 MPa, D_1=0. Additionally, in order to reduce the calculation cost, a 15 g-18 ms constant acceleration is applied to the piston and the cylinder base of the TWG to simulate the pre-pressured gas in the chamber. The drop height of the table is converted into the initial velocity (2.75 m/s with downward direction) assigned on the TWG, and the fixed boundary condition is assigned on the bottom of the impact hammer. The dynamic explicit solver (with time step of 1×10^{-6} s) is employed to calculate the acceleration-time curve during the whole shock test, and the time period is set as 0.03 s.

7

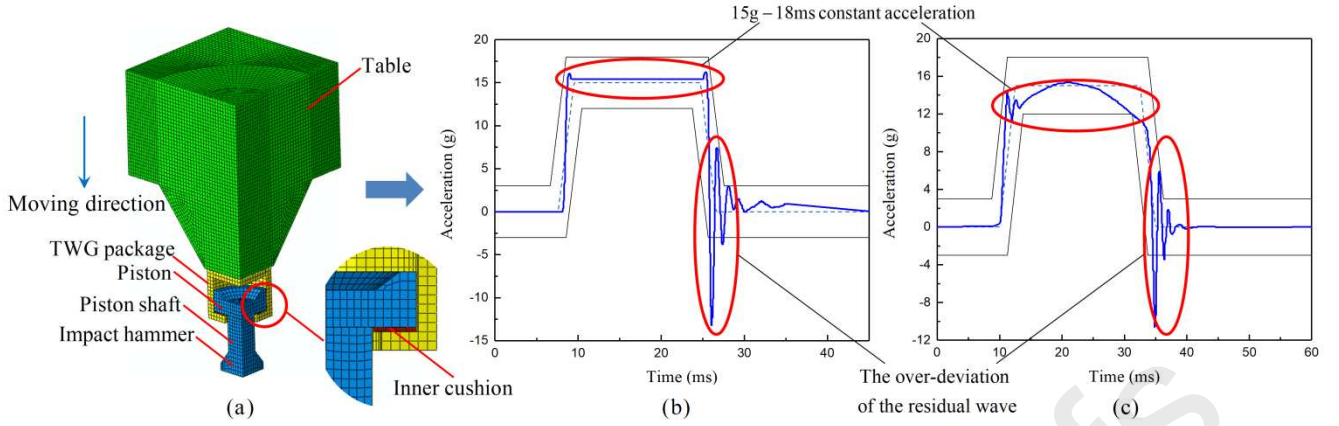Fig. 8. FEM analysis of the TWG. Shown in the figure are (a) the FEM model of the TWG and the table of the drop shock tester (the quarter model with symmetric boundary conditions is displayed), (b) the simulated shock waveform, and (c) the experimental shock waveform.

Table 1. Material assignments and mesh characteristics of the FEM model.

Parameters	Components					
	Table	TWG package	Piston	Piston shaft	Impact hammer	Inner cushion
Material type	aluminium alloy	alloy steel	aluminium alloy	aluminium alloy	aluminium alloy	rubber
Elastic modulus (GPa)	69	210	69	69	69	—
Density (kg/m³)	2810	7800	2810	2810	2810	1000
Poisson's ratio	0.330	0.300	0.330	0.330	0.330	—
Grid size	61788	714	540	385	375	72
Element type	C3D8R	C3D8R	C3D8R	C3D8R	C3D8R	C3D8R

The governing equation of the FEM model is

$$M^{\mathrm{e}}\ddot{x}^{\mathrm{e}} + C^{\mathrm{e}}\dot{x}^{\mathrm{e}} + K^{\mathrm{e}}x^{\mathrm{e}} = Q, \tag{3}$$

where, M^{e}, C^{e}, and K^{e} are the mass matrix, the damping matrix, and the stiffness matrix of the FEM model respectively; Q represents the external force vector (containing the contact force); $\ddot{x}^{\mathrm{e}}$, $\dot{x}^{\mathrm{e}}$, x^{e} are the acceleration vector, the velocity vector, and the displacement vector of the FEM model respectively. The central difference algorithm is utilized to calculate Eq.(3), and the explicit iteration can be expressed as [28]

$$\left(\frac{1}{\Delta t^2}M^{\mathrm{e}} + \frac{1}{2\Delta t}C^{\mathrm{e}}\right)x^{\mathrm{e}}_{t+\Delta t} = Q_t - \left(K^{\mathrm{e}} - \frac{2}{\Delta t^2}M^{\mathrm{e}}\right)x^{\mathrm{e}}_t - \left(\frac{1}{\Delta t^2}M^{\mathrm{e}} - \frac{1}{2\Delta t}C^{\mathrm{e}}\right)x^{\mathrm{e}}_{t-\Delta t}, \tag{4}$$

where Δt is the time step; $x^{\mathrm{e}}_{t+\Delta t}$, x^{e}_t, and $x^{\mathrm{e}}_{t-\Delta t}$ are the displacement vector at time $t+\Delta t$, t, and $t-\Delta t$; Q_t is the external force vector at time t. The explicit method guarantees the calculation convergence. The given time step satisfies the requirements of Eq. (5), which guarantees the calculation stability synchronously [27].

$$\begin{cases} \Delta t_{\mathrm{stable}} \leq \frac{L^{\mathrm{e}}_{\min}}{C_{\mathrm{d}}} \\ C_{\mathrm{d}} = \sqrt{\frac{E_{\mathrm{M}}}{\rho_{\mathrm{M}}}} \end{cases}, \tag{5}$$

where, $L^{\mathrm{e}}_{\min} = 5$ mm is the minimum mesh size of the FEM model; C_{d} is the material wave velocity; E_{M} and ρ_{M} are the elastic modulus and the density of the material assigned to the FEM model respectively. In this work, two kinds of material, i.e. aluminium alloy and alloy steel, are used to construct the FEM model, and, thusly, $C_{\mathrm{d}} \approx 5000$ m/s can be figured out.

The calculated acceleration-time curve is presented in Fig. 8(b). The comparison between Fig. 8(b) and Fig.

8(c) shows that the simulated shock pulse has a similar trend to the experimental result, illustrating the validity and accuracy of the FEM simulation. Particularly, in the portion of the oscillation wave at the end of the descending ramp, the simulated residual wave is almost in accordance with the experimental result, which verifies the proposed hypothesis that the over deviation of the residual wave is posed by the collision of the piston against the end cover of the TWG.

3. Dynamics modeling and impact intensity solution for the terminal impact of TWG

3.1 Dynamics modeling for the impact between the piston and the end cover

In this section, a 1D continuous rod model is established to describe the longitudinal impact between the piston and the end cover of the TWG. As shown in Fig. 9, the impact system is simplified for dynamics modeling. In Fig. 9, the piston shaft is modeled as a rod; the impact hammer and the piston are simplified as the lumped mass attached on the down and upper ends of the rod respectively; and the inner cushion is equivalent to a spring. Based on the longitudinal vibration theory of 1D continuous rod, it is considered that the cross section of the rod is always planar; the stress distribution on the rod interface is uniform; and the gravity of each part can be ignored [30]. In this model, the piston, piston shaft, and the impact hammer will together impact the equivalent spring with an initial velocity, and the pressure of the equivalent spring equals the impact force.
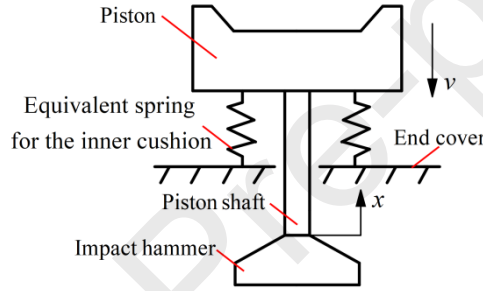
Fig. 9. The simplified impact system for the terminal impact of TWG.

In this model, the length of the piston shaft is denoted by l; the cross-section area of the piston shaft is denoted by A; the density of the piston shaft is represented by ρ; the elastic modulus of the piston shaft is expressed as E; the mass of the piston and the impact hammer are represented by m and M respectively; and the stiffness of the equivalent spring is denoted by k. The down end of the piston shaft is set as the origin of the coordinate, and, meanwhile, without loss of generality, the upward direction is defined as the positive direction. Correspondingly, the governing equation, the boundary condition, and the initial condition for describing the longitudinal impact behavior between the piston and the end cover can be established and expressed as follows:

The governing equation is

$$\frac{\partial^2 u(x,t)}{\partial t^2} = c^2 \frac{\partial^2 u(x,t)}{\partial x^2}, \tag{6}$$

where, $u(x,t)$ is the longitudinal vibration displacement of the rod (piston shaft) at time t and $c^2 = \frac{E}{\rho}$ is the specific stiffness of the rod.

The boundary condition can be expressed as

$$\begin{cases} EA\frac{\partial u(0,t)}{\partial x} = M\frac{\partial^2 u(0,t)}{\partial x^2} \\ EA\frac{\partial u(l,t)}{\partial x} + ku(l,t) + m\frac{\partial^2 u(l,t)}{\partial x^2} = 0 \end{cases}. \tag{7}$$

The initial condition is

9

$$\begin{cases} u(x, 0) = 0 \\ \frac{\partial u(x,0)}{\partial t} = -v, \end{cases} \tag{8}$$

where, v is the initial impact velocity of the piston.

To further simplify these equations, Eq.(6)-(8) can be non-dimensionalized respectively by setting $\zeta = \frac{x}{l}$, $\tau = \frac{ct}{l}$, $\tilde{k} = \frac{kl}{EA}$, $\alpha = \frac{\rho Al}{M}$, $\eta = \frac{m}{\rho Al}$, and $\tilde{u}(\zeta, \tau) = \frac{cu(x,t)}{vl}$ [31].

Consequently, the governing equation is converted to

$$\frac{\partial^2 \tilde{u}(\zeta, \tau)}{\partial \tau^2} = \frac{\partial^2 \tilde{u}(\zeta, \tau)}{\partial \zeta^2}. \tag{9}$$

The boundary condition is simplified as

$$\begin{cases} \alpha \frac{\partial \tilde{u}(0,\tau)}{\partial \zeta} = \frac{\partial^2 \tilde{u}(0,\tau)}{\partial \tau^2} \\ \frac{\partial \tilde{u}(1,\tau)}{\partial \zeta} + \tilde{k}\tilde{u}(1,\tau) + \eta \frac{\partial^2 \tilde{u}(1,t)}{\partial \tau^2} = 0 \end{cases}. \tag{10}$$

Similarly, the initial condition can be non-dimensionalized as

$$\begin{cases} \tilde{u}(\zeta, 0) = 0 \\ \frac{\partial \tilde{u}(\zeta, 0)}{\partial \tau} = -1 \end{cases}. \tag{11}$$

3.2 Solution for the dynamics model

In this section, the mode superposition method is used to solve the established dynamics model in section 3.1. The method of separation of variables is used in this work by setting $\tilde{u}(\zeta, \tau) = U(\zeta)T(\tau)$ [32], and the separated results can be expressed as follows:

$$\ddot{U}(\zeta) + \lambda^2 U(\zeta) = 0; \tag{12}$$

$$\ddot{T}(\tau) + \lambda^2 T(\tau) = 0; \tag{13}$$

$$\alpha \dot{U}(0) + \lambda^2 U(0) = 0; \tag{14}$$

$$\dot{U}(1) + \tilde{k}U(1) - \eta \lambda^2 U(1) = 0. \tag{15}$$

In Eq.(12)-(15), λ is non-dimensional natural frequency, and the general solution of the principal modes can be expressed as

$$U(\zeta) = \tilde{A}\cos(\lambda \zeta) + \tilde{B}\sin(\lambda \zeta), \tag{16}$$

where, $\tilde{A}$ and $\tilde{B}$ are the amplitudes of the principal modes. Substituting Eq.(16) into Eq.(14) and Eq.(15) gives

$$\begin{cases} \tilde{A}\lambda^2 + \alpha \tilde{B}\lambda = 0 \\ \tilde{B}[(\tilde{k} - \eta \lambda^2)\sin(\lambda) + \lambda \cos(\lambda)] = \tilde{A}[\lambda \sin(\lambda) - (\tilde{k} - \eta \lambda^2)\cos(\lambda)] \end{cases}. \tag{17}$$

Then, the frequency equation can be figured out from Eq.(17), which can be expressed as:

$$\lambda \tan(\lambda) = \frac{\alpha(\tilde{k} - \eta \lambda^2) - \lambda^2}{\alpha + \tilde{k} - \eta \lambda^2}. \tag{18}$$

Besides, the principal mode function, i.e. Eq.(16), of each order can be figured out from Eq.(16)-(18), which can be expressed as:

$$U_i(\zeta) = \cos(\lambda_i \zeta) - \frac{\lambda_i}{\alpha}\sin(\lambda_i \zeta), \ i = 1, 2, \dots, n. \tag{19}$$

Similarly, the time function, i.e. Eq.(13), of each order can also be derived as:

$$T_i(\tau) = \tilde{C}_i \cos(\lambda_i \tau) + \tilde{D}_i \sin(\lambda_i \tau), \ i = 1, 2, \dots, n, \tag{20}$$

in which, $\tilde{C}_i$ and $\tilde{D}_i$ are the amplitudes of the i-th time function. Lastly, the vibration displacement of the rod can be

10

obtained with the mode superposition method, i.e.,

$$\tilde{u}(\zeta, \tau) = \sum_{i=1}^{n} U_i(\zeta)T_i(\tau) = \sum_{i=1}^{n}\left[\cos(\lambda_i\zeta) - \frac{\lambda_i}{\alpha}\sin(\lambda_i\zeta)\right]\left[\tilde{C}_i\cos(\lambda_i\tau) + \tilde{D}_i\sin(\lambda_i\tau)\right]. \tag{21}$$

3.3 Solution for the orthogonality of the principal modes

Obviously, it can be found that the variables $\tilde{C}_i$ and $\tilde{D}_i$ in Eq.(21) should be determined prior to calculating the vibration displacement. To this end, the orthogonality of the principal modes should be calculated beforehand. Suppose that $U_i(\zeta)$ and $U_j(\zeta)$ are the principal mode with the non-dimensional natural frequency λ_i and λ_j respectively. It can be obtained from Eq.(12) that:

$$\begin{cases} \ddot{U}_i(\zeta) = -\lambda_i^2 U_i(\zeta) \\ \ddot{U}_j(\zeta) = -\lambda_j^2 U_j(\zeta) \end{cases}. \tag{22}$$

Multiplying U_i and U_j and integrating the product from 0 to 1 gives

$$\int_0^1 \ddot{U}_i U_j \mathrm{d}\zeta = -\lambda_i^2 \int_0^1 U_i U_j \mathrm{d}\zeta. \tag{23}$$

Meanwhile, with the method of integration by parts, Eq.(23) can also be expressed as:

$$\int_0^1 \ddot{U}_i U_j \mathrm{d}\zeta + \int_0^1 \dot{U}_i \dot{U}_j \mathrm{d}\zeta + \left(\tilde{k} - \eta\lambda_i^2\right) U_i(1)U_j(1) = \frac{\lambda_i^2}{\alpha}U_i(0)U_j(0). \tag{24}$$

Combining Eq.(23) and (24) gives

$$\lambda_i^2 \int_0^1 \left[U_i U_j + \frac{1}{\alpha}U_i(0)U_j(0) + \eta U_i(1)U_j(1)\right]\mathrm{d}\zeta = \tilde{k}U_i(1)U_j(1) + \int_0^1 \dot{U}_i \dot{U}_j \mathrm{d}\zeta. \tag{25}$$

In the same way, Eq.(23) can also be simplified as

$$\lambda_j^2 \int_0^1 \left[U_j U_i + \frac{1}{\alpha}U_j(0)U_i(0) + \eta U_j(1)U_i(1)\right]\mathrm{d}\zeta = \tilde{k}U_j(1)U_i(1) + \int_0^1 \dot{U}_j \dot{U}_i \mathrm{d}\zeta. \tag{26}$$

Eq.(25) subtracting Eq.(26) gives

$$\begin{cases} \int_0^1 [\alpha + \delta(\zeta) + \alpha\eta\delta(\zeta-1)]U_i(\zeta)U_j(\zeta)\mathrm{d}\zeta = \begin{cases} 0, & i \neq j \\ \beta_i, & i = j \end{cases} \\ \beta_i = \frac{\alpha^2 + \lambda_i^2}{2\alpha} + \cos^2(\lambda_i) + \frac{\alpha^2 - \lambda_i^2}{4\alpha\lambda_i}\sin(2\lambda_i) + \alpha\eta\left[\cos(\lambda_i) - \frac{\lambda_i}{\alpha}\sin(\lambda_i)\right]^2 \end{cases}. \tag{27}$$

Note that, in Eq.(27), $\delta(\cdot)$ is the Dirac delta function; $\lambda_i^2 \neq \lambda_j^2$ when $i \neq j$.

3.4 Solution for the impact force and the impact duration

Substituting Eq.(21) into Eq.(11), the initial condition can be expressed as

$$\begin{cases} \tilde{u}(\zeta, 0) = \sum_{i=1}^{n} \tilde{C}_i\left[\cos(\lambda_i\zeta) - \frac{\lambda_i}{\alpha}\sin(\lambda_i\zeta)\right] = 0 \\ \frac{\partial \tilde{u}(\zeta, 0)}{\partial \tau} = \sum_{i=1}^{n} \tilde{D}_i\lambda_i\left[\cos(\lambda_i\zeta) - \frac{\lambda_i}{\alpha}\sin(\lambda_i\zeta)\right] = -1 \end{cases}. \tag{28}$$

In Eq.(28), $\tilde{C}_i$ and $\tilde{D}_i$ can be figured out by utilizing the orthogonality of the principal modes. Multiplying both sides of Eq.(28) by $[\alpha + \delta(\zeta) + \alpha\eta\delta(\zeta-1)]U_i(\zeta)$, and, then, integrating from 0 to 1 gives

$$\begin{cases} \tilde{C}_i = 0 \\ \tilde{D}_i = -\frac{(1+\alpha\eta)\lambda_i\cos(\lambda_i) + (\alpha - \eta\lambda_i^2)\sin(\lambda_i)}{\beta_i\lambda_i^2} \end{cases}. \tag{29}$$

Substituting Eq.(29) into Eq.(21), the non-dimensional vibration displacement can be figured out as

$$\tilde{u}(\zeta, \tau) = \sum_{i=1}^{n} \tilde{D}_i\sin(\lambda_i\tau)\left[\cos(\lambda_i\zeta) - \frac{\lambda_i}{\alpha}\sin(\lambda_i\zeta)\right], \tag{30}$$

and, thus, the vibration displacement of the rod at $x=l$ can be calculated analytically, i.e.,

11

$$u(l, t) = \frac{vl}{c} \sum_{i=1}^{n} \tilde{D}_i \sin\left(\frac{\lambda_i c}{l} t\right) \left[\cos(\lambda_i) - \frac{\lambda_i}{\alpha} \sin(\lambda_i)\right]. \tag{31}$$

Therefore, the impact force F can be calculated with the pressure of the equivalent spring, i.e.,

$$F = -ku(l, t) = -k\frac{vl}{c} \sum_{i=1}^{n} \tilde{D}_i \sin\left(\frac{\lambda_i c}{l} t\right) \left[\cos(\lambda_i) - \frac{\lambda_i}{\alpha} \sin(\lambda_i)\right]. \tag{32}$$

Obviously, the impact process will stop when $F=0$, and, hence, the impact duration T_F can be obtained by solving the equation $u(l, T_F) = 0$.

4. Case study

In this section, a real TWG is used to study the structural parameters of TWG on the impact force and the impact duration. The material distribution of the TWG is that the impact hammer, the piston rod, and the piston are manufactured with aluminium alloy; the inner cushion is made with polyurethane; and the rest of the TWG is fabricated with alloy steel. The main structural parameters and their values in this case are presented in Table 2. Note that, in Table 2, the cross-section area A of the piston shaft is determined by its diameter (denoted as d) because the piston shaft is majorly designed as a cylinder. The equivalent stiffness k can be calculated as follows: suppose that the thickness of the inner cushion is l_I; the elastic modulus of the inner cushion is E_I; the Poisson's ratio of the inner cushion is υ; the number of the inner cushions is n_I; and the effective contact area of the inner cushion is A_I. The generalized Hooke law is:

$$\begin{cases} \varepsilon_r = \frac{1}{E_I}[\sigma_r - \upsilon(\sigma_\theta + \sigma_z)] \\ \varepsilon_\theta = \frac{1}{E_I}[\sigma_\theta - \upsilon(\sigma_r + \sigma_z)], \\ \varepsilon_z = \frac{1}{E_I}[\sigma_z - \upsilon(\sigma_\theta + \sigma_r)] \end{cases} \tag{33}$$

where ε_r, ε_θ, and ε_z are the strain of the inner cushion in the radial, the tangential, and the axial directions respectively; σ_r, σ_θ, and σ_z are the stress of the inner cushion in the radial, the tangential, and the axial directions respectively. Considering that in the actual working process of TWG, the inner cushion is fixed on the end cover, and, thus, can neither expand along the radial direction nor rotate around the axial direction, but only deform along the axial direction. Thusly, setting $\varepsilon_r=\varepsilon_\theta=0$, Eq.(33) can be simplified as

$$\varepsilon_z = \frac{\sigma_z}{E_I}\left(\frac{1 - \upsilon - 2\upsilon^2}{1 - \upsilon}\right). \tag{34}$$

Without considering the plastic deformation or the material damage, the inner cushion can be treated as linear elastic material, and, hence, the equivalent stiffness of the inner cushion can be expressed as:

$$k = n_I \frac{E_I A_I}{l_I}\left(\frac{1 - \upsilon}{1 - \upsilon - 2\upsilon^2}\right). \tag{35}$$

The polyurethane material is widely used for the inner cushion, and, generally, $E_I \approx 3.6$ GPa, $\upsilon \approx 0.3$ [33]. The remaining parameters in Eq.(35), i.e. n_I, l_I, and A_I, should be adjusted on a case-by-case basis. In this case, $n_I=4$, $l_I=10$ mm, $A_I \approx 1.3 \times 10^6$ mm^2, and, correspondingly, $k=1.218 \times 10^9$ N/m. Additionally, the initial impact velocity of the piston against the end cover can be extracted from the FEM model that equals 2.5 m/s approximately.

Table 2. Structural and kinematic parameters of the TWG.

Parameters	l (mm)	d (mm)	ρ (kg/m³)	E (GPa)	m (kg)	M (kg)	k (N/m)	v (m/s)
Values	120	85	2810	69	2.53	7.77	1.218×10^9	2.5

Substituting the parameters in Table 2 into Eq.(18), the non-dimensional natural frequency λ can be figured out with one-dimensional search methods, and the searching model can be expressed as:

12

$$\begin{cases} \min f(\lambda) = \left| \lambda \tan(\lambda)(\alpha + \tilde{k} - \eta\lambda^2) - \alpha(\tilde{k} - \eta\lambda^2) + \lambda^2 \right| \\ \lambda_i \in [L_i, U_i], \quad i = 1, 2, \ldots, n \end{cases} , \tag{36}$$

where $[L_i, U_i]$ is the search range for the i-th non-dimensional natural frequency. In this work, the former 10-order natural frequencies are used to calculate the vibration displacement and the impact force. In this case, the former 10-order non-dimensional natural frequencies are listed in Table 3. Then, substituting these natural frequencies into Eq.(32), the impact force can be calculated and shown in Fig. 10.

Table 3. The former 10-order non-dimensional natural frequencies.

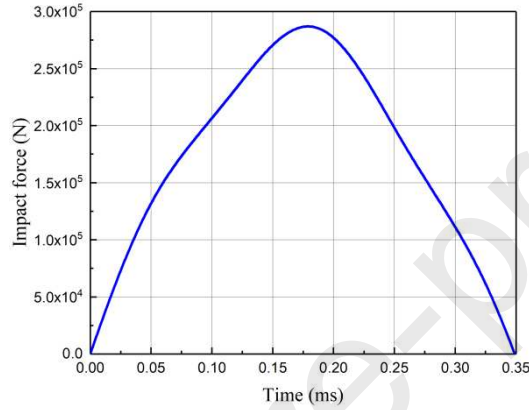| λ_i	λ_1	λ_2	λ_3	λ_4	λ_5	λ_6	λ_7	λ_8	λ_9	λ_{10}
Values	0.221	1.025	3.435	6.439	9.530	12.646	15.772	18.903	22.037	25.173

Fig. 10. The impact force-time curve. In this figure, the amplitude is 2.869×10^5 N, and the duration is 0.350 ms.

5. Parameters analysis

As analyzed in section 2, the essential strategy for alleviating the over deviation phenomenon in the residual wave is reducing the impact force and the impact duration as much as possible. Therefore, in this section, through combining the calculation method in section 4, the effects of several parameters, including the impact velocity, the attached mass, the piston weight, the equivalent stiffness of the inner cushion, the length of the piston rod, and the diameter of the piston rod, on the impact force and the impact duration are investigated and discussed.

5.1 The effect of the impact velocity on the impact force and impact duration

In order to investigate the effect of the impact velocity on the impact force and the impact duration, the impact velocity v is set as 1.0 m/s, 1.5 m/s, 2.0 m/s, 2.5 m/s, and 3.0 m/s to calculate the impact force curve respectively. The remaining parameters in Table 2 are kept frozen. The calculated impact force curves at different impact velocities are demonstrated in Fig. 11. The amplitudes $F_{\max}$ and the durations T_F of these impact force-time curves are listed in Table 4.
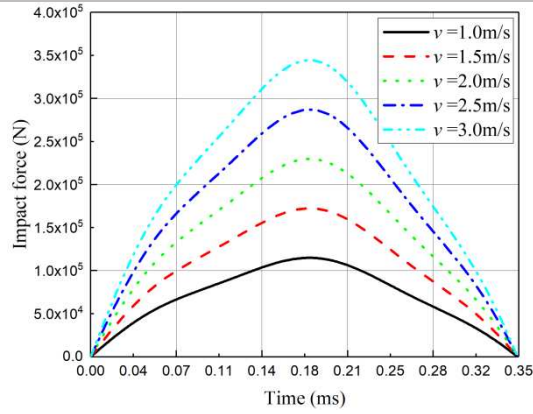
13

Fig. 11. The impact force-time curves at different impact velocities.

Table 4. The amplitudes and the durations at different impact velocities

Indicators	v (m/s)				
	1.0	1.5	2.0	2.5	3.0
F_{max} (N)	1.148×10^5	1.721×10^5	2.295×10^5	2.869×10^5	3.443×10^5
T_F(ms)	0.350	0.350	0.350	0.350	0.350

It can be found from Fig. 11 and Table 4 that the impact force increases with the increment of the impact velocity, and the increasing trend almost remains linear. This trend is also consistent with the characteristic contained in Eq.(32). Nevertheless, the impact duration keeps constant at different impact velocities. The reason is that the impact velocity has no effect on the natural frequencies, and, hence, T_F is constant. These two characteristics can be observed from Eq.(18) and Eq.(31).

5.2 The effect of the attached mass on the impact force and impact duration

Similarly, to investigate the effect of the attached mass, i.e. the mass of the impact hammer, on the impact force and the impact duration, the attached mass M is set as 1.77 kg, 3.77 kg, 5.77 kg, 7.77 kg, and 9.77 kg to calculate the impact force curve respectively. The remaining parameters in Table 2 are kept frozen. The calculated impact force curves at different attached masses are displayed in Fig. 12. The amplitudes F_{max} and the durations T_F of these impact force-time curves are listed in Table 5. Note that, in this condition, the former 10-order natural frequencies will be varied with different attached masses. The varied former 10-order natural frequencies at different attached masses are listed in Table 6.
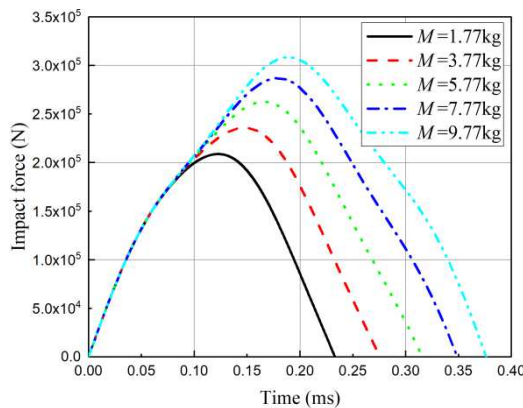

Fig. 12. The impact force-time curves at different attached masses.

14

Table 5. The amplitudes and the durations at different attached masses.

Indicators	M (kg)				
	1.77	3.77	5.77	7.77	9.77
F_{max} (N)	2.088×10^5	2.359×10^5	2.625×10^5	2.869×10^5	3.083×10^5
T_F (ms)	0.235	0.277	0.317	0.350	0.378

Table 6. The former 10-order non-dimensional natural frequencies at different attached masses.

M (kg)	λ_1	λ_2	λ_3	λ_4	λ_5	λ_6	λ_7	λ_8	λ_9	λ_{10}
1.77	0.326	1.302	3.640	6.562	9.615	12.711	15.824	18.946	22.074	25.206
3.77	0.277	1.131	3.503	6.478	9.557	12.666	15.788	18.916	22.048	25.183
5.77	0.244	1.062	3.458	6.452	9.539	12.652	15.777	18.907	22.041	25.176
7.77	0.221	1.025	3.435	6.439	9.530	12.646	15.772	18.903	22.037	25.173
9.77	0.203	1.002	3.422	6.431	9.525	12.642	15.768	18.900	22.034	25.171

It can be found from Fig. 12 and Table 5 that the impact force and the impact duration both increase with the increment of the attached mass and present as diagram so that the linear trend can be seen. According to Eq.(32), these variation trends are due to the changes of the attached mass, which will cause changes in the natural frequencies and the vibration modes of the impact system. Meanwhile, it can be observed from Table 6 that with the increasing of the attached mass, the natural frequency of the same order decreases, resulting in the increment of the impact duration. However, with the increase of the frequency order, the frequency values are less sensitive to the change of the attached mass, so that the frequency values of different orders at different attached masses are very close to each other. Actually, with the increase of the attached mass, the proportion of low-frequency components (especially the first-order frequency) in the vibration displacement response keeps increasing, leading to the continuous increase of the amplitude of the impact force.

5.3 The effect of piston weight on the impact force and impact duration

On the other hand, in order to investigate the effect of the piston weight on the impact force and the impact duration, the piston mass m is set as 0.53 kg, 2.53 kg, 4.53 kg, 6.53 kg, and 8.53 kg to calculate the impact force-time curve respectively. The remaining parameters in Table 2 are kept frozen. The calculated impact force-time curves at different piston weights are presented in Fig. 13. The amplitudes F_{max} and the durations T_F of these impact force-time curves are listed in Table 7. Note that, similarly, in this condition, the former 10-order natural frequencies will be varied with different piston weights. The varied former 10-order natural frequencies at different piston weights are listed in Table 8.
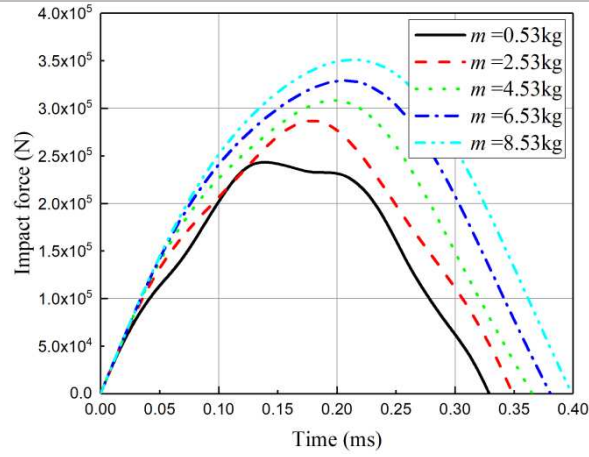
15

Fig. 13. The impact force-time curves at different piston weights.

Table 7. The amplitudes and the durations at different piston weights.

Indicators	m (kg)				
	0.53	2.53	4.53	6.53	8.53
F_{max} (N)	2.432×10^5	2.869×10^5	3.081×10^5	3.290×10^5	3.510×10^5
T_F (ms)	0.330	0.350	0.367	0.382	0.400

Table 8. The former 10-order non-dimensional natural frequencies at different piston weights.

m (kg)	λ_1	λ_2	λ_3	λ_4	λ_5	λ_6	λ_7	λ_8	λ_9	λ_{10}
0.53	0.234	1.545	3.984	6.819	9.807	12.861	15.947	19.050	22.164	25.285
2.53	0.221	1.025	3.435	6.439	9.530	12.646	15.772	18.903	22.037	25.173
4.53	0.209	0.849	3.343	6.388	9.495	12.619	15.750	18.885	22.022	25.159
6.53	0.199	0.759	3.305	6.368	9.482	12.609	15.742	18.878	22.016	25.154
8.53	0.189	0.703	3.285	6.357	9.474	12.604	15.738	18.874	22.013	25.151

It can be found from Fig. 13 and Table 7 that the impact force and the impact duration both increase with the increment of the piston weight, and the increasing trend almost remains linear too. According to Eq.(32), similar to the analysis in section 5.2, these variation trends are due to the changes of the piston weight, which will cause changes in the natural frequencies and the vibration modes of the impact system. Actually, with the increase of the piston weight, the impact kinetic energy increases, leading to the larger impact force and the longer impact duration. Meanwhile, the changing trends of the frequencies in Table 8 are also similar to that in section 5.2.

5.4 The effect of equivalent stiffness of the inner cushion on the impact force and impact duration

In order to investigate the effect of the equivalent stiffness of the inner cushion on the impact force and the impact duration, the equivalent stiffness k is set as 3.045×10^8 N/m, 6.090×10^8 N/m, 9.135×10^8 N/m, 1.218×10^9 N/m, and 1.522×10^9 N/m to calculate the impact force-time curve respectively. The remaining parameters in Table 2 are kept frozen. The calculated impact force-time curves at different equivalent stiffness levels are presented in Fig. 14. The amplitudes F_{max} and the durations T_F of these impact force curves are listed in Table 9. Note that, similarly, in this condition, the former 10-order natural frequencies will be varied with different equivalent stiffness levels. The varied former 10-order natural frequencies at different equivalent stiffness are
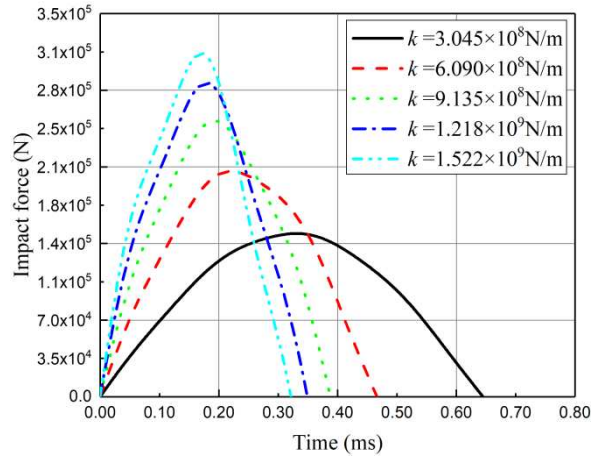
listed in Table 10.

Fig. 14. The impact force-time curves at different equivalent stiffness levels of the inner cushion.

Table 9. The amplitudes and the durations at different equivalent stiffness levels of the inner cushion.

Indicators	k (N/m)				
	3.045×10^8	6.090×10^8	9.135×10^8	1.218×10^9	1.522×10^9
F_{max} (N)	1.491×10^5	2.060×10^5	2.521×10^5	2.869×10^5	3.139×10^5
T_F (ms)	0.646	0.468	0.390	0.350	0.323

Table 10. The former 10-order non-dimensional natural frequencies at different equivalent stiffness levels of the inner cushion.

k (N/m)	λ_1	λ_2	λ_3	λ_4	λ_5	λ_6	λ_7	λ_8	λ_9	λ_{10}
3.045×10^8	0.118	0.959	3.431	6.439	9.530	12.646	15.772	18.903	22.037	25.173
6.090×10^8	0.163	0.981	3.433	6.439	9.530	12.646	15.772	18.903	22.037	25.173
9.135×10^8	0.195	1.003	3.434	6.439	9.530	12.646	15.772	18.903	22.037	25.173
1.218×10^9	0.221	1.025	3.435	6.439	9.530	12.646	15.772	18.903	22.037	25.173
1.522×10^9	0.241	1.047	3.436	6.439	9.530	12.646	15.772	18.903	22.037	25.173

It can be found from Fig. 14 and Table 9 that the impact force increases with increasing equivalent stiffness levels, but, on the contrary, the impact duration decreases with the increase of the equivalent stiffness. According to Eq.(32), the increase of the equivalent stiffness will increase the natural frequency of the impact system of each order, and the corresponding vibration period of each order will be shorter, thus making the impact duration shorter. Meanwhile, when the equivalent stiffness is small, the inner cushion is soft, so that it will lead the unidirectional compression effect of the contact medium (the inner cushion) to be more obvious than the longitudinal vibration effect of the piston rod, and so as to make 1) the piston displacement larger, 2) the impact duration longer, 3) the amplitude of the impact force lower, and 4) the curve of the impact force more gradual.

5.5 The effect of non-dimensional parameters $\alpha, \eta, \tilde{k}$ on the impact force and impact duration

Before analyzing the effects of the piston rod length and the piston rod diameter, the effects of three non-dimensional parameters, α, η, and $\tilde{k}$, on the impact force and impact duration should be studied. Since α, η, and $\tilde{k}$ are all non-dimensional parameters, the impact force and impact duration should also be non-dimensionalized correspondingly. To this end, assuming $\tilde{F} = \frac{FC}{EAv}$, Eq.(32) can be converted into

$$\tilde{F} = -\tilde{k}\sum_{i=1}^{n}\tilde{D}_i\sin(\tau)\left[\cos(\lambda_i) - \frac{\lambda_i}{\alpha}\sin(\lambda_i)\right], \tag{37}$$

where $\tilde{F}$ is the non-dimensional impact force, and $\tau = \frac{ct}{l}$ is the non-dimensional parameter representing the impact duration. The initial values of α, η, and $\tilde{k}$ can be determined based on parameters in Table 2, which are 0.246, 1.322, and 0.373 respectively.

In this section, α is firstly set as 0.15, 0.20, 0.25, 0.30, and 0.35 (initial values of η and $\tilde{k}$ are kept frozen) to calculate the corresponding impact force-time curves respectively. Then, similarly, η is set as 0.05, 1.00, 1.50, 2.00, and 2.50 (initial values of α and $\tilde{k}$ are kept frozen) to calculate the corresponding impact force-time curves respectively. Lastly, $\tilde{k}$ is set as 0.20, 0.30, 0.40, 0.50, and 0.60 (initial values of α and η are kept frozen) to calculate the corresponding impact force-time curves respectively. The calculated impact force-time curves at different α, η, $\tilde{k}$ are demonstrated in Fig. 15-17 respectively. The amplitudes $F_{\max}$ and the durations T_F of these impact force curves are listed in Table 11-13.
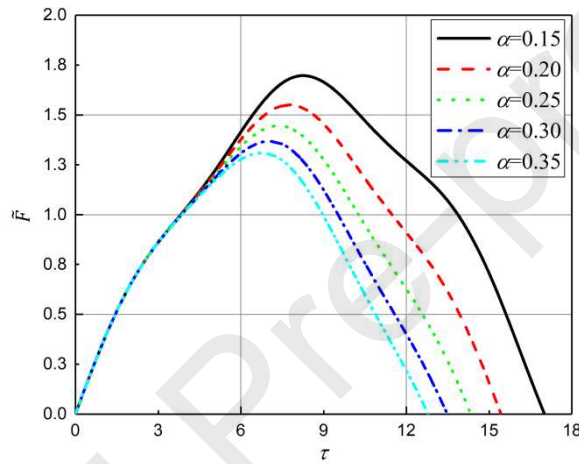

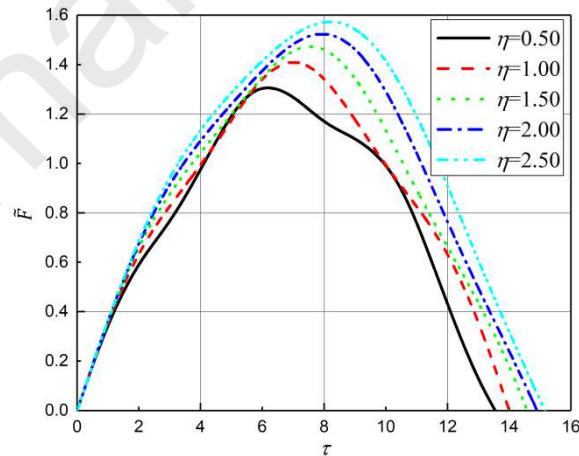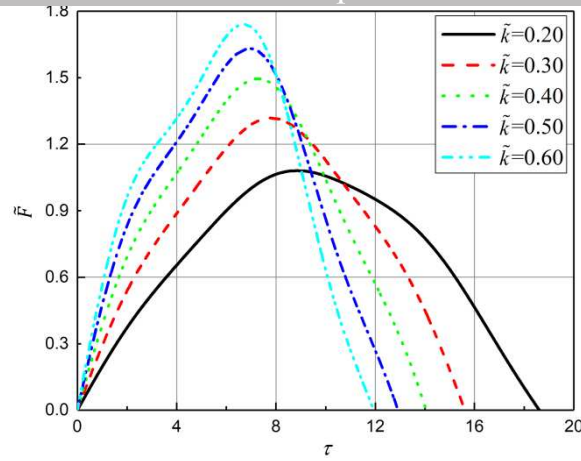Fig. 15. The impact force-time curves at different α's.

Fig. 16. The impact force-time curves at different η's.

18

Fig. 17. The impact force-time curves at different $\tilde{k}$'s.

Table 11. The amplitudes and the durations at different α's.

Indicators	α				
	0.15	0.20	0.25	0.30	0.35
$\tilde{F}$	1.697	1.551	1.446	1.368	1.309
τ	17.011	15.432	14.339	13.486	12.799

Table 12. The amplitudes and the durations at different η's.

Indicators	η				
	0.50	1.00	1.50	2.00	2.50
$\tilde{F}$	1.305	1.409	1.473	1.524	1.573
τ	13.548	14.003	14.582	14.904	15.158

Table 13. The amplitudes and the durations at different $\tilde{k}$'s.

Indicators	$\tilde{k}$				
	0.20	0.30	0.40	0.50	0.60
$\tilde{F}$	1.080	1.318	1.495	1.631	1.740
τ	18.610	15.612	14.054	12.919	11.937

It can be found from Fig. 15 and Table 11 that both the impact force and the impact duration increase with the decrement of α. Since $\alpha = \frac{\rho A l}{M}$ is the ratio of the piston rod mass, $\rho A l$, to the mass of the impact hammer, M, the decrease of α implies the increase of the impact hammer's mass w.r.t the mass of the piston rod. Therefore, in accordance with the conclusion in section 5.2, the decrease of α would result in the increases of both the impact force and impact duration.

From Fig. 16 and Table 12, it can be found that both the impact force and the impact duration increase with the increasement of η. Similarly, as $\eta = \frac{m}{\rho A l}$ represents the ratio of the piston mass, m, to the piston rod mass, $\rho A l$, the increase of η brings the increase of piston mass w.r.t the piston rod mass, and, consequently, arouses both the increased impact force and impact duration, according to the conclusion in section 5.3. However, it can be

19

observed from Fig. 16 that the rising trends of the impact force and impact duration are not prominently sensitive to the increase of η.

Additionally, it can be found from Fig. 17 and Table 13 that the impact force increases and the impact duration decreases with increasing $\tilde{k}$. $\tilde{k} = \frac{kl}{EA}$ represents the ratio of the stiffness of the equivalent spring, k, to the stiffness of the rod, $\frac{EA}{l}$. Similar to the conclusion in section 5.4, as shown in Table 14, the increased $\tilde{k}$ results in higher natural frequencies, and, thusly, shortens the main vibration period under each natural frequency, such that the impact duration becomes shorter. Meanwhile, the smaller $\tilde{k}$ implies a softer inner cushion and a harder piston rod, which will lead to the effect of unidirectional compression of the inner cushion that is more prominent than the effect of longitudinal vibrations of the piston rod, hence prolonging the impact duration and decreasing the impact amplitude.

Table 14. The former 10-order non-dimensional natural frequencies at different $\tilde{k}$'s.

$\tilde{k}$	λ_1	λ_2	λ_3	λ_4	λ_5	λ_6	λ_7	λ_8	λ_9	λ_{10}
0.20	0.168	0.984	3.433	6.439	9.530	12.646	15.772	18.903	22.037	25.173
0.30	0.201	1.008	3.434	6.439	9.530	12.646	15.772	18.903	22.037	25.173
0.40	0.227	1.032	3.435	6.439	9.530	12.646	15.772	18.903	22.037	25.173
0.50	0.248	1.055	3.437	6.439	9.530	12.646	15.772	18.903	22.037	25.173
0.60	0.265	1.079	3.438	6.440	9.530	12.646	15.772	18.903	22.0367	25.173

5.6 The effect of the piston rod length on the impact force and impact duration

Also, for investigating the effect of the the piston rod length on the impact force and the impact duration, the length of the piston rod l is set as 40 mm, 80 mm, 120 mm, 160 mm, and 200 mm to calculate the impact force curves respectively. The remaining parameters in Table 2 are kept frozen. The calculated impact force curves at different lengths are presented in Fig. 18. The amplitudes F_{max} and the durations T_F of these impact force curves are listed in Table 15. Note that, similarly, in this condition, the former 10-order natural frequencies will be varied with different lengths. The varied former 10-order natural frequencies at different lengths are listed in Table 16.
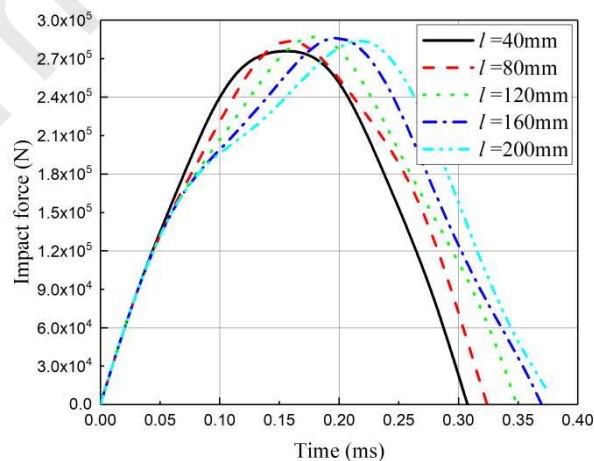

Fig. 18. The impact force-time curves at different lengths of the piston rod.

Table 15. The amplitudes and the durations at different lengths of the piston rod.

Indicators	l (mm)				
	40	80	120	160	200

F_{max} (N)	2.759×10^5	2.837×10^5	2.869×10^5	2.862×10^5	2.839×10^5
T_F (ms)	0.309	0.326	0.350	0.371	0.383

Table 16. The former 10-order non-dimensional natural frequencies at different lengths of the piston rod.

l (mm)	λ_1	λ_2	λ_3	λ_4	λ_5	λ_6	λ_7	λ_8	λ_9	λ_{10}
40	0.082	0.584	3.245	6.336	9.460	12.593	15.729	18.867	22.006	25.146
80	0.155	0.832	3.342	6.388	9.495	12.619	15.750	18.885	22.022	25.159
120	0.221	1.025	3.435	6.439	9.530	12.646	15.772	18.903	22.037	25.173
160	0.279	1.190	3.524	6.490	9.565	12.672	15.793	18.920	22.052	25.186
200	0.333	1.334	3.610	6.540	9.599	12.698	15.814	18.938	22.067	25.199

It can be found from Fig. 18 and Table 15 that the amplitudes of the impact force are not very sensitive to the change of the length of the piston rod. A longer rod will lead to an increase in the mass of the piston rod but a decrease in the stiffness of the piston rod simultaneously, hence decreased η but increased α and $\tilde{k}$. However, the effects of increasing α and decreasing η on the impact force are opposite to increasing $\tilde{k}$, and, meanwhile, it can be found from Fig. 15-17 that the effects of increasing α and decreasing η on the impact force are both less sensitive than increasing $\tilde{k}$. Therefore, with the increased piston rod length, the impact force varies slightly and even is reduced to a certain extent. Another tendency can be concluded from Fig. 18 and Table 15 is that the impact duration increases with the increment of the length of piston rod. The reason is that, when the length of the piston rod increases, the initial momentum of the system increases, and when the amplitude of the impact force is constant, the impact duration will be longer. Besides, since $t=\frac{l\tau}{c}$, it can also be found that the increase of l will lead to the amplification of impact duration.

5.7 The effect of the piston rod diameter on the impact force and impact duration

Lastly, for investigating the effect of the diameter of the piston rod on the impact force and the impact duration, the diameter of the piston rod d is set as 5 mm, 45 mm, 85 mm, 125 mm, and 165 mm to calculate the impact force-time curves respectively; the remaining parameters in Table 2 are kept frozen. The calculated impact force-time curves at different diameters are presented in Fig. 19. The amplitudes F_{max} and the durations T_F of these impact force-time curves listed in Table 17. Note that, similarly, in this condition, the former 10-order natural frequencies will be varied with different diameters. The varied former 10-order natural frequencies at different diameters are listed in Table 18.
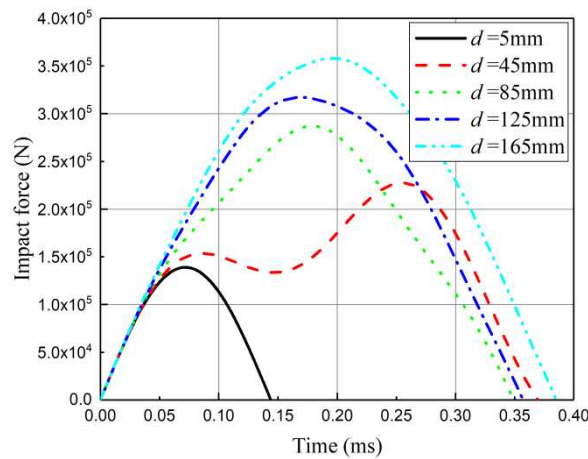

Fig. 19. The impact force-time curves at different diameters of the piston rod.

Table 17. The amplitudes and the durations at different diameters of the piston rod.

Indicators	d (mm)				
	5	45	85	125	165
$F_{\max}$ (N)	1.389×10^5	2.273×10^5	2.869×10^5	3.171×10^5	3.579×10^5
T_{F} (ms)	0.145	0.371	0.350	0.359	0.387

Table 18. The former 10-order non-dimensional natural frequencies at different diameters of the piston rod.

d (mm)	λ_1	λ_2	λ_3	λ_4	λ_5	λ_6	λ_7	λ_8	λ_9	λ_{10}
5	0.029	0.534	3.143	6.284	9.425	12.567	15.708	18.850	21.991	25.133
45	0.189	0.705	3.230	6.328	9.455	12.589	15.726	18.864	22.004	25.144
85	0.221	1.025	3.435	6.439	9.530	12.646	15.772	18.903	22.037	25.173
125	0.214	1.343	3.707	6.608	9.648	12.736	15.845	18.964	22.089	25.219
165	0.198	1.621	3.997	6.817	9.803	12.857	15.943	19.047	22.161	25.282

It can be found from Fig. 19 and Table 17 that, overall, the larger the piston rod diameter is, the greater the impact force is, and the shorter the impact duration is. According to the conclusion in section 5.5, the increased diameters will lead to the decreases of η and $\tilde{k}$ and increased α, which would further result in the reduction of $\tilde{F}$. However, from $F = \frac{\pi E c \tilde{F}}{4C} d^2$, it can be found that $\tilde{F}$ will be magnified by d^2, which consequently leads to the amplification of the impact force. On the other hand, the increase of α and the decrease of η will arouse the reduction of the impact duration, but the decrease of $\tilde{k}$ will increase the impact time. It can be found from Fig. 15-17 that the effects of increasing α and decreasing η on the impact duration are both less sensitive than decreasing $\tilde{k}$. Therefore, the impact duration will also be longer with the increased piston rod diameter.

Besides, an outlier shown in Fig. 19 is that, when d=45 mm, the impact force-time curve does not have a single peak, but shows a waveform with two peaks and asymmetric with time. With the aim to analyze this "two peaks" phenomenon in detail, the 10-order mode shapes at different piston rod diameters are decomposed and demonstrated in Fig. 20. It can be found from Fig. 20(b) that, when d=45 mm, the first and second mode shapes are both dominant (the rest mode shapes can be negligible), and the superposition of the first and second mode shapes results in the "two peaks" phenomenon in Fig. 19. However, when d=85 mm, 125 mm, or 165 mm, it can be found from Fig. 20(c)-(e) that only the first mode shapes are dominant, and, thusly, the final impact force-time curves are all similar to the half-sine curve. Similarly, it can be seen from Fig. 20(a) that, when d=5 mm, there is only the second mode shape in dominance, which also leads to the final modal superposition result similar to the half-sine curve. Additionally, as shown in Fig. 21, the influence of the piston rod diameters on the pulse shape of the impact force-time curves is further investigated. It can be observed from Fig. 21 that this "two peaks" phenomenon does not only exist at d=45 mm but will reoccur when d=25-65 mm.

22
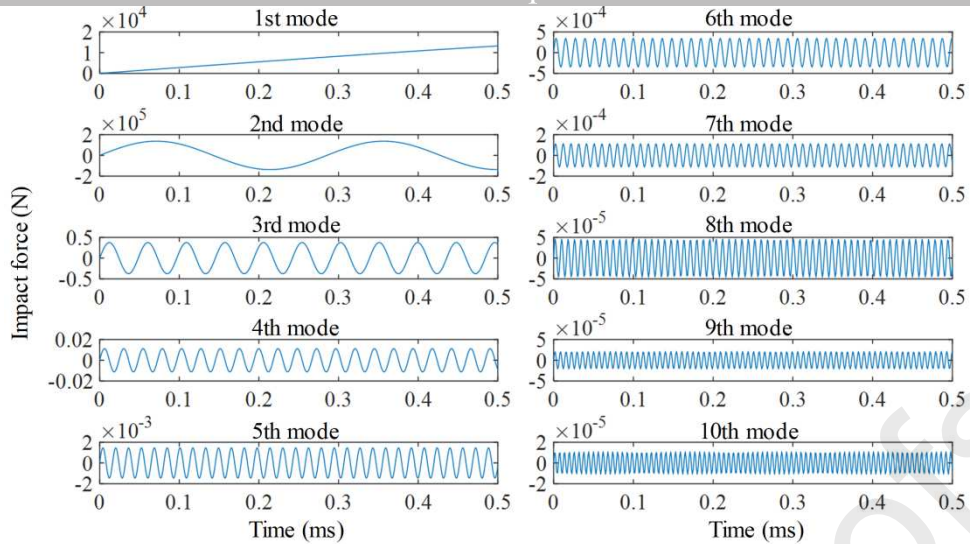
(a) $d = 5$mm

(b) $d = 45$mm

(c) $d = 85$mm
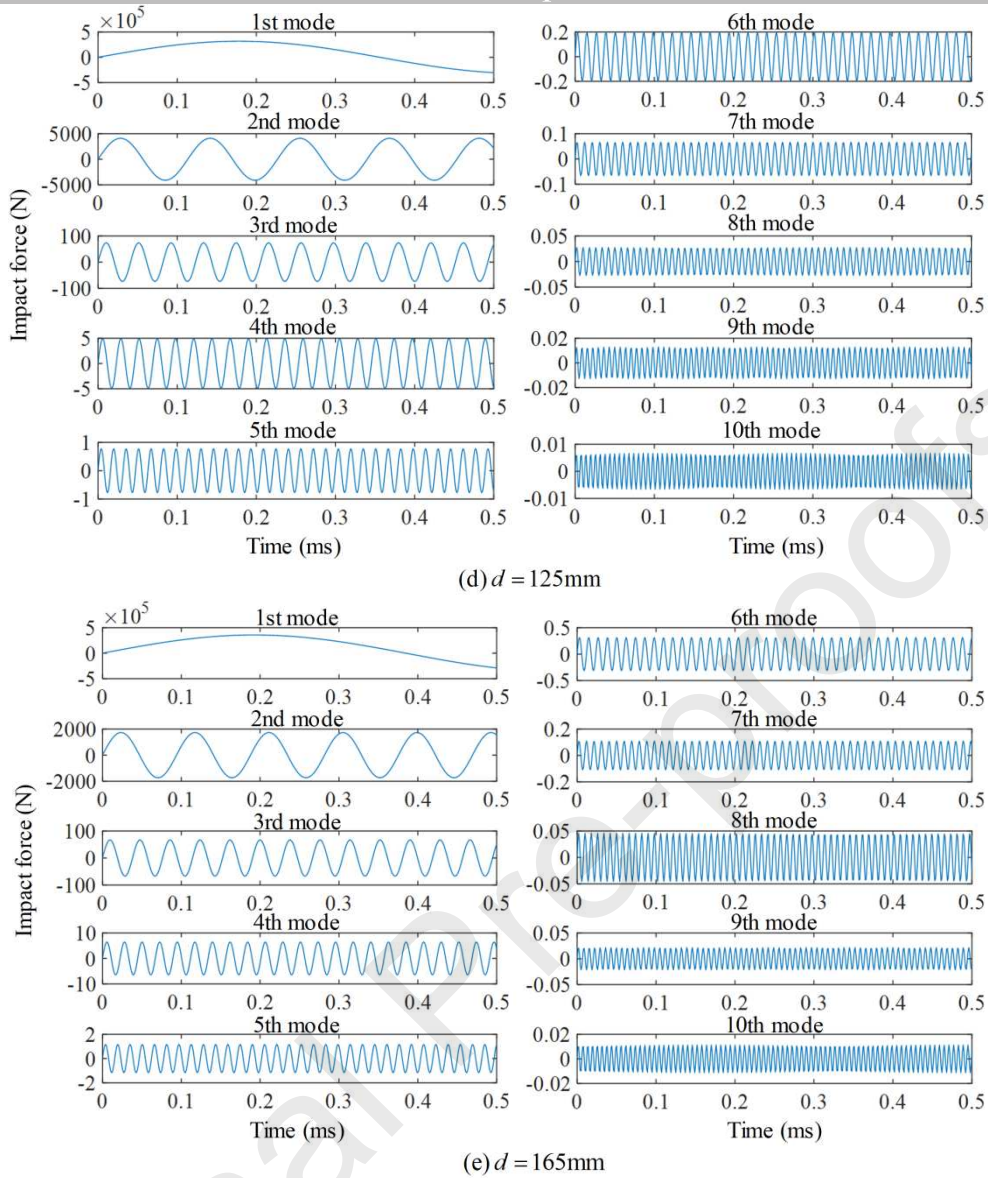
(d) $d = 125$mm
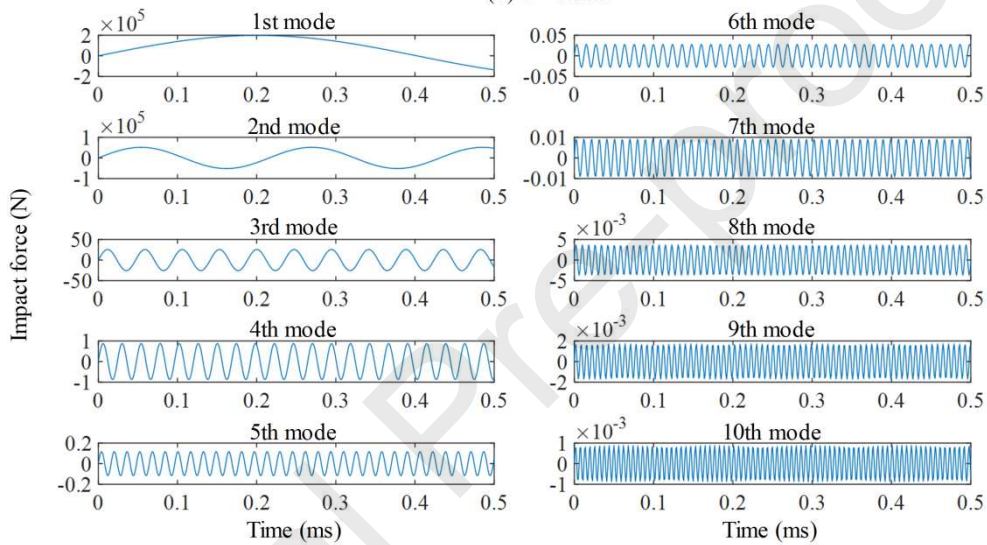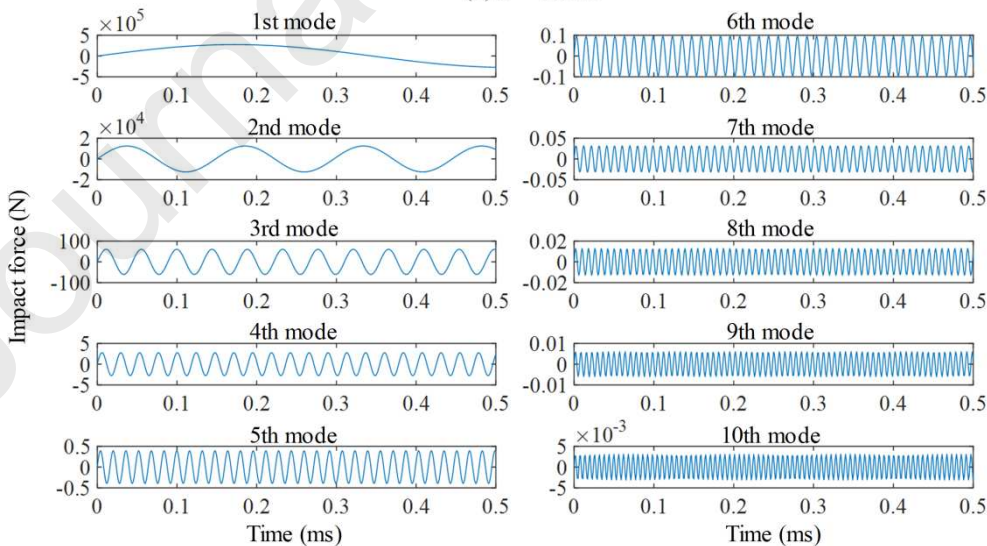
(e) $d = 165$mm

Fig. 20. The former 10-order mode shapes at different diameters of the piston rod.
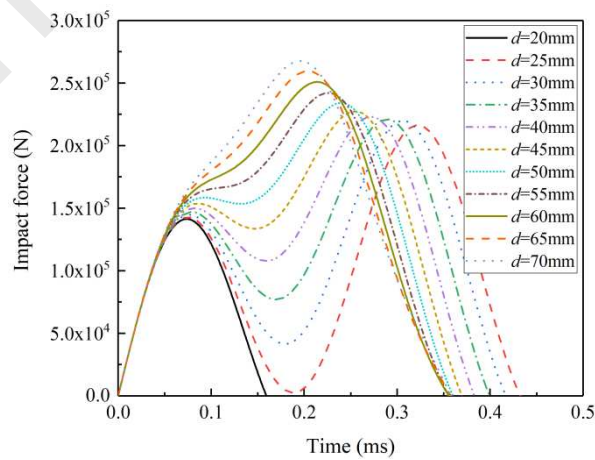

Fig. 21. The impact force-time curves at different piston rod diameters.

6. Structural optimization of the TWG

In this section, a series of measures are proposed to optimize the structure of the TWG based on the analysis

24

in section 5.

In accordance with the analyzed results in section 5, it can be concluded that the most effective measures for reducing the impact force of the piston against the end cover of the TWG include minimizing the impact velocity, reducing the mass of the impact hammer, lessening the mass of the piston, minishing the stiffness of the inner cushion, and decreasing the diameter of the piston rod. However, considering practical engineering requirements, parts of the proposed measures are not available. Firstly, owing to that the impact velocity between the piston and the end cover is derived by the initial drop height of the TWG, and, based on Eq.(2), the initial drop height determines the pulse amplitude and the pulse duration of the generated trapezoidal shock waveform, so it is almost impermissible to alleviate the impact force through reducing the impact velocity. Secondly, considering that the piston is the main bearing component during the shock test process, lessening the mass of the piston would pose the reduction of the piston's strength, and, thus, it is limited to mitigate the impact force via decreasing the mass of the piston. Lastly, although reducing the stiffness of the inner cushion, for example using softer material, can lower the impact force to some extent, the concomitant longer impact duration would be detrimental for the structural protection of the TWG. Therefore, it is not a good strategy to alleviate the impact force by considerable reduction on the equivalent stiffness of the inner cushion.

Consequently, there are two key parameters, which are the mass of the impact hammer and the diameter of the piston rod, available to optimize. According to the analysis in section 5.2 and 5.7, with aim to alleviate the impact force, the mass of the impact hammer and the diameter of the piston rod should be reduced as much as possible. However, a similar problem still exists is that the reduction of the diameter will decrease the strength of piston rod. In this work, in order to reduce the mass of the impact hammer and the diameter of the piston rod to the greatest extent, while maintaining sufficient strength of the TWG, a kind of separate-style structure is modified for the TWG. As shown in Fig. 22, the piston rod and the impact hammer are separated from the piston. These optimized measures are equivalent to reduce the impact hammer mass, the piston rod diameter, and the piston rod length all to 0. So, w.r.t the structural parameters of the traditional TWG in Table 2, the structural parameters of the optimized separate-style TWG can be summarized in Table 19.
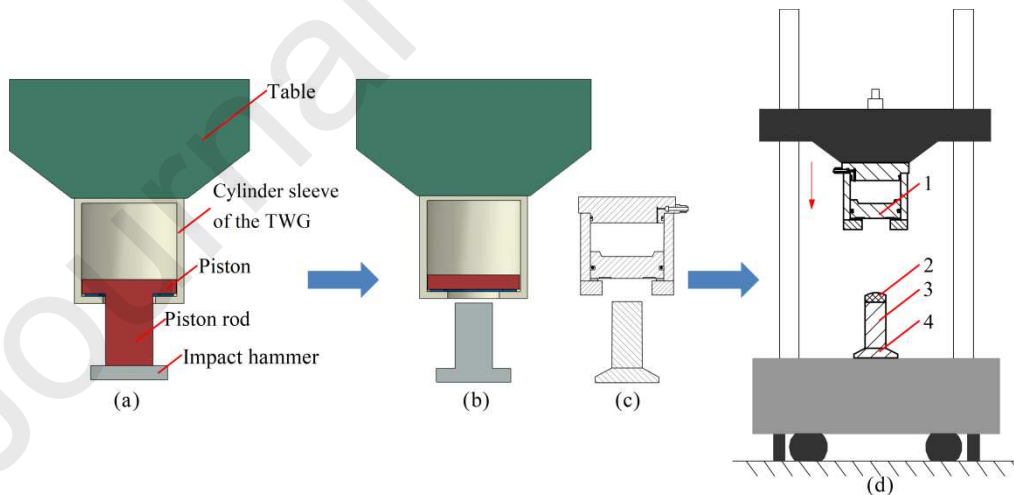

Fig. 22. The separate-style TWG. Shown in the figure are (a) the traditional TWG, (b) the optimized separate-style TWG, (c) the schematic of the mechanical structure of the optimized TWG, and (d) the schematic of the practical working mode of the optimized TWG in shock test. The components indexed in (d) are 1-piston, 2-rubber cushion, 3-piston rod, and 4-impact hammer.

Table 19. Structural parameters of the optimized separate-style TWG.

Parameters	l (mm)	d (mm)	ρ (kg/m^3)	E (GPa)	m (kg)	M (kg)	k (N/m)
Values	0	0	2810	69	2.53	0	1.218×10^9

For further illustrate the rationality of these optimization measures, we substitute d=0.1 mm, l=0.001 mm, M=0.001 kg (simulating the condition of d=0, l=0, and M=0) into Eq.(32) (the remaining parameters are kept the same with the results in Table 2) to calculate the impact intensity of the separate-style TWG in shock tests. The calculated impact force is depicted in Fig. 23. Comparing the impact force-time curves shown in Fig. 10 and Fig. 23, it can be found that the impact intensity of the optimized separate-style TWG in shock tests is alleviated to a great extent (both the amplitude and the duration are reduced by more than 50% w.r.t the result in Fig. 10), which illustrates the designing rationality of the separate-style TWG.
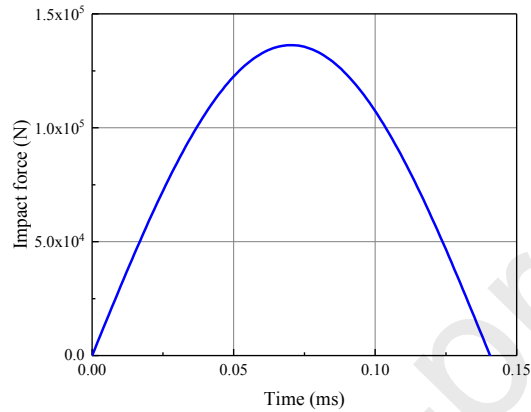

Fig. 23. The impact force-time curve. In this figure, the amplitude is 1.363×10^5 N, and the duration is 0.142 ms.

As shown in Fig. 24, a separate-style TWG is manufactured based on the proposed measures, and practical shock tests are conducted with this optimized TWG. In these shock tests, a piezoelectric accelerometer (YMC 221A25 with calibrated sensitivity of 29.8 PC/g and measuring range of $\pm$2000 g [34]), which can be used to measure the shock signals, is mounted on the table of the drop shock tester (SY10-100 [35]). The accelerometer is connected to the charge amplifier with a signal cable. The measured electrical signals from the accelerometer will be transmitted to the data acquisition system after amplification by the charge amplifier. The sampling time and the sampling frequency of the data acquisition system is 800 ms and 48 kHz respectively, and, hence, a total of 36800 sampling points can be acquired in each shock test, which ensures the high fidelity of the measured shock data. Finally, the acquired shock signals can be demonstrated on the monitor after tailoring and filtering treatments. As shown in Fig. 3, the tailoring treatment would reserve the main shock pulse portion with $2.4T_D$ and cut off the remaining sampling points according to IEC 60068-2-27-2008 [6]. The low-pass filtering is applied to eliminate high-frequency noise hidden in the measured shock signals, and the cut-off frequency can be determined as $\frac{10}{T_D}$ according to the JESD22-B104-A [8].
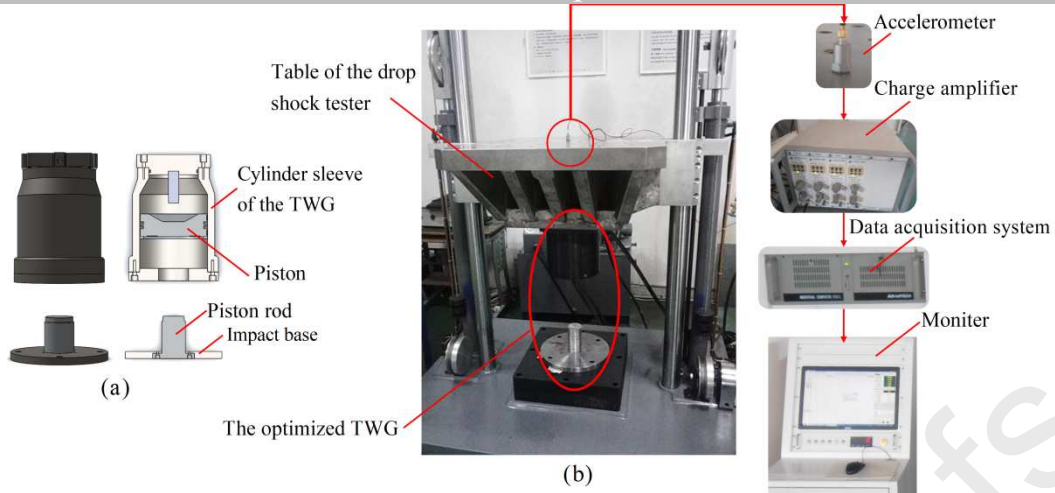
Fig. 24. The experimental shock tests with the optimized TWG. Shown in the figure are (a) the CAD drawings of the optimized separate-style TWG, and (b) the shock test system with the optimized TWG.

Six experimental trapezoidal shock waveforms generated with the optimized TWG are presented in Fig. 25, of which every shock test repeated at least three times to validate the high repeatability of the measuring results. Taking the measured results at the 50 g-11 ms condition as the example, as shown in Table 20, the measured results of these three-times shock tests are highly consistent, illustrating the high repeatability of the optimized TWG and this shock test system. It can be found from Fig. 25 that the over deviation phenomenon of the residual wave can be alleviated effectively, and the acquired trapezoidal shock waveforms can meet the tolerance requirements of the IEC standards satisfactorily [6]. These experimental results verify the effectiveness of the optimized TWG.

Table 20. The measured results of the repeated shock tests (three times) at the 50 g-11 ms condition. In this Table, the peak acceleration is the maximum acceleration of the measured shock pulse; the pulse width is obtained at 10% the peak based on the JEDEC definition [8]; the velocity variation can be calculated by integrating the whole acceleration-time curve; and the mean acceleration is the average of the all the sampling points of the measured shock pulse.

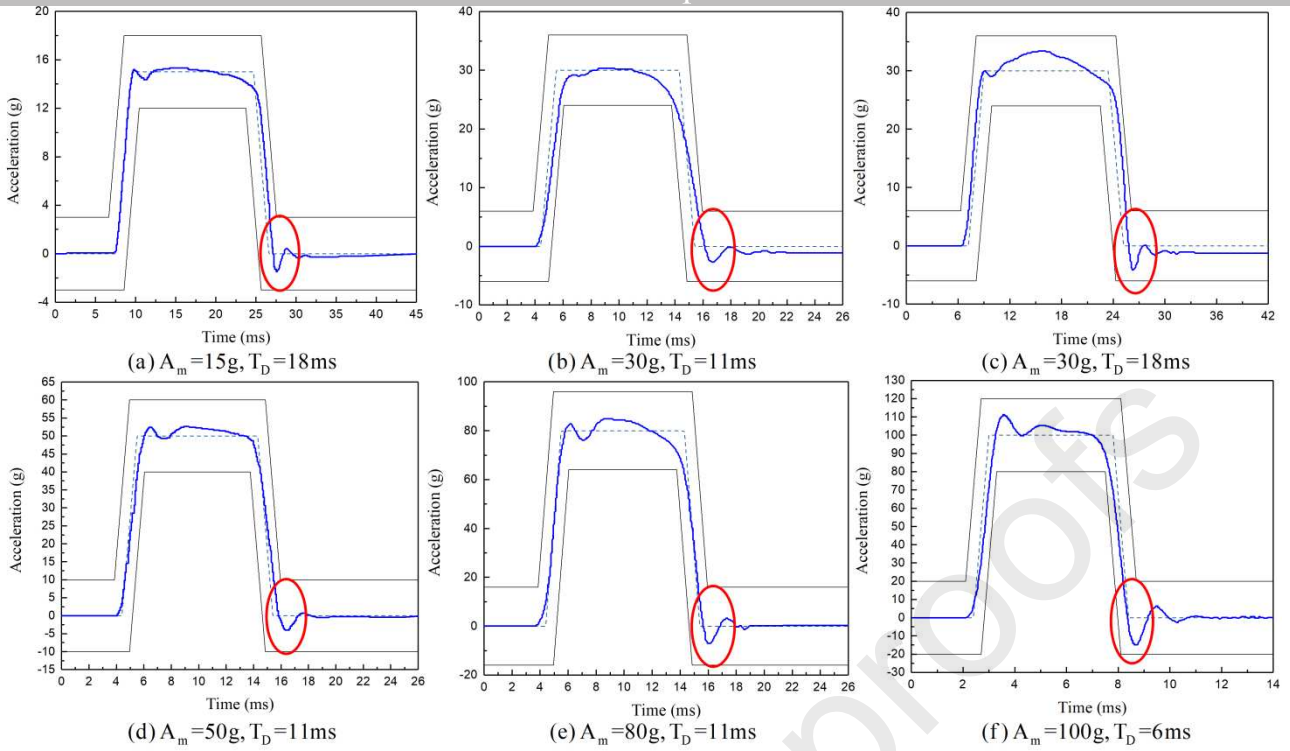| Sequence	Peak acceleration (g)	Pulse width (ms)	Velocity variation (m/s)	Mean acceleration (g)	Passing the tolerance?
1	54.80	11.13	5.49	44.07	Yes
2	54.81	11.17	5.51	44.05	Yes
3	54.68	11.21	5.52	43.96	Yes

Fig. 25. The experimental results of the shock tests with the optimized TWG.

For further illustrate the rationality of the hypothesis that the over deviation is caused by the impact between the piston and the end cover of the TWG, as shown in Fig. 26(a), the FEM simulation is conducted under the same conditions as the FEM model shown in Fig. 8(a). The calculated acceleration-time curve is displayed in Fig. 26(b). Fig. 26(c) is the experimental result, which is identical to Fig. 25(a). The comparison between Fig. 26(b) and Fig. 26(c) shows that the simulated trapezoidal shock waveform has an identically consistent trend with the experimental result. This verifies the validity of the FEM model again. Besides, the over deviation phenomenon of the residual waves of the simulated shock pulse and the experimental result are considerably similar, illustrating the rationality of the hypothesis that the over deviation of the residual wave is posed by the impact between the piston and the end cover of the TWG further. Additionally, the comparison between Fig. 8(a) and Fig. 26(b) illustrates that the over deviation phenomenon can be alleviated by optimizing the traditional TWG as this separate-style structure.
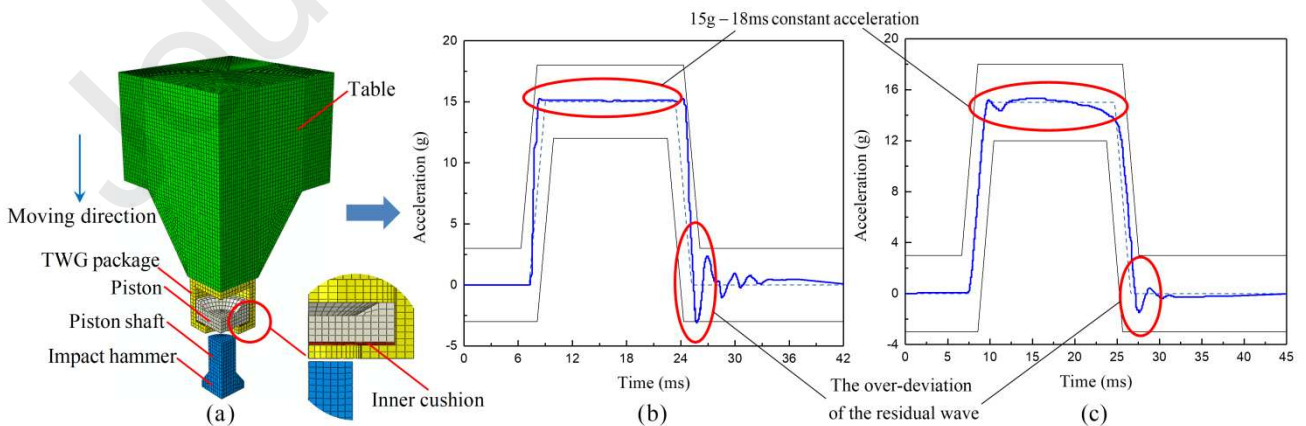

Fig. 26. FEM analysis of the separate-style TWG. Shown in the figure are (a) the FEM model of the separate-style TWG and the table of the drop shock tester, (b) the simulated shock waveform, and (c) the experimental shock waveform.

7. Conclusion

Over deviation of the residual wave in trapezoidal shock waveform generation is concerned in this work. Through dynamic analysis and FEM simulation, it is hypothesized and verified that the over deviation phenomenon of residual waves is caused by the impact between the piston and the end cover of the TWG at the end of the shock test.

Then, according to this hypothesis, a 1D continuous rod-based dynamics model is established based on the longitudinal vibration theory of continuous system to describe the impact behavior between the piston and the end cover of the TWG. The analytic expression for calculating the impact force and the impact duration caused by the impact between the piston and the end cover can be established based on this 1D continuous rod-based dynamics model and the mode superposition method. The equivalent stiffness of the inner cushion can be formulated with the Hooke law theory by simplifying the inner cushion as an equivalent spring. Finally, the impact force and the impact duration can be calculated quantitatively by substituting specific structural and kinematic parameters into the established analytic expression.

The effects of several structural parameters, including the impact velocity, the attached mass, the piston weight, the stiffness of the inner cushion, the piston rod length, and the piston rod diameter, of the TWG on the impact force and the impact duration are analyzed based on the calculation of the proposed 1D continuous rod-based dynamics model. The analyzed conclusion is that 1) the impact force increases with the increment of the impact velocity, but the impact duration keeps constant at different impact velocities; 2) the impact force and the impact duration both increase with the increment of the attached mass; 3) the impact force increases with increasing equivalent stiffness, but the impact duration decreases with the increase of the equivalent stiffness; 4) the impact duration increases with the increment of the length of piston rod, but the amplitude of the impact force is not very sensitive to the change of the piston rod length; and 5) the larger the piston rod diameter is, the greater the impact force is, and the shorter the impact duration is. Also, corresponding explanations are given for these conclusions respectively. Particularly, before explaining the effects of the piston rod length and the piston rod diameter, the effects of three non-dimensional parameters, α, η and $\tilde{k}$, are analyzed in detail. For explaining the occurred "two peaks" phenomenon in the analysis of the effects of different diameters, the 10-order mode shapes at different piston rod diameters are demonstrated and studied specifically. These analysis results would be constructive for the structure optimization of TWG.

Lastly, combining the consideration on these analysis results and practical requirements of shock tests, the structure of the TWG is optimized by separating the piston and the piston rod, which is equivalent to reducing the impact hammer mass, the piston rod diameter, and the piston rod length to 0. The calculated impact force-time curve of the optimized separate-style TWG shows that the impact intensity between the piston and the end cover can be alleviated to a great extent through these optimization measures. Several shock tests are conducted with the designed separate-style TWG, and the experimental results show that optimized TWG can alleviate the over deviation phenomenon and generate adequate trapezoidal shock waveforms effectively. Lastly, a FEM simulation is applied on the separate-style TWG, which illustrates the rationality of the proposed hypothesis in section 2.2 again. These structural modifications for TWG are easy to implement and conduct for the shock tests which need to generate satisfactory trapezoidal shock waveforms.

However, it should be noted that this optimized TWG needs to be installed at the bottom of the table of the drop shock tester, which weakens the load capacity of the drop shock tester to a certain extent. Moreover, this separate-style TWG poses a little assembly complexity, e.g. the piston rod needs to be adjusted repeatedly to align with the center of the piston before implementing a shock test. Therefore, the further study will be concentrated on how to improve the load capacity and the operating convenience of the optimized TWG. Additionally, the inner cushion is assumed as an elastomer in this work, which facilitates the solving of the impact intensity of the

collision between the piston and the end cover. For describing the impact between the piston and the end cover more precisely, in the future study, the plastic deformation of the inner cushion should be considered to further improve the dynamics model of the terminal impact of the TWG.

CRediT authorship contribution statement

Jingjing Wen: Conceptualization, Funding acquisition, Investigation, Methodology, Visualization, Writing-original draft. **Houpu Yao:** Formal analysis, Writing-review & editing. **Bin Wu:** Resources, Supervision. **Ze Ji:** Software, Writing-review & editing. **Lihua Wen:** Project administration. **Man Xu** and **Yi Jin:** Software, Validation. **Xunliang Yan:** Resources, Funding acquisition, Supervision.

Declaration of competing interest

The authors declare that there are no conflicts of interest regarding the publication of this paper.

Acknowledgments

References

[1] Wu, M. L., & Lan, J. S. (2018). Reliability and failure analysis of SAC 105 and SAC 1205N lead-free solder alloys during drop test events. *Microelectronics Reliability, 80*, 213-222.

[2] Shi, J., He, Q., & Wang, Z. (2021). An LSTM-based severity evaluation method for intermittent open faults of an electrical connector under a shock test. *Measurement, 173*, 108653.

[3] Wen, J., Yao, H., Ji, Z., Wu, B., & Xu, F. (2021). Self-validating high-g accelerometers through data-driven methods. *Sensors and Actuators A: Physical, 328*, 112803.

[4] Wu, I. C., Wang, M. H., & Jang, L. S. (2018). Experimental location of damage in microelectronic solder joints after a board level reliability evaluation. *Engineering Failure Analysis, 83*, 131-140.

[5] Wen, J., Yao, H., Ji, Z., Wu, B., & Xia, M. (2021). On fault diagnosis for high-g accelerometers via data-driven models. *IEEE Sensors Journal*, *21*(2), 1359-1368.

[6] IEC 60068-2-27-2008. *Environmental testing - Part 2-27: Tests-Test Ea and guidance: Shock.*

[7] ANSI/EIA 364-27C-2011. *Mechanical Shock (Specified Pulse) Test Procedure for Electrical Connectors and Sockets.*

[8] Wen, J., Liu, C., Yao, H., & Wu, B. (2018). A nonlinear dynamic model and parameters identification method for predicting the shock pulse of rubber waveform generator. *International Journal of Impact Engineering, 120*, 1-15.

[9] Wu, B., Liu, C., & Wen, J. (2017, October). The optimized algorithm for working parameters of the vertical impact testing machine. In *2017 13th IEEE International Conference on Electronic Measurement & Instruments (ICEMI)* (pp. 424-430). IEEE.

[10] Yan, Y., & Li, Q. M. (2019). Low-pass-filter-based shock response spectrum and the evaluation method of transmissibility between equipment and sensitive components interfaces. *Mechanical Systems and Signal Processing, 117*, 97-115.

[11] Jung, B. H., Kim, Y. W., Lee, J. R., & Kim, D. S. (2019). Visualization of pyroshock wave reduction by insulator using a laser shock based simulation method. *Measurement, 137*, 302-311.

[12] García-Pérez, A., Sorribes-Palmer, F., Alonso, G., & Ravanbakhsh, A. (2019). FEM simulation of space instruments subjected to shock tests by mechanical impact. *International Journal of Impact Engineering, 126*, 11-26.

[13] Garcia-Perez, A., Sorribes-Palmer, F., Alonso, G., & Ravanbakhsh, A. (2018). Overview and application of FEM methods for shock analysis in space instruments. *Aerospace Science and Technology, 80*, 572-586.

[14] Younis, M. I., Jordy, D., & Pitarresi, J. M. (2007). Computationally efficient approaches to characterize the dynamic response of

microstructures under mechanical shock. *Journal of Microelectromechanical Systems*, *16*(3), 628-638.

[15] Iqbal, M. Z., & Israr, A. (2021). To predict a shock pulse using non linear dynamic model of rubber waveform generator. *International Journal of Impact Engineering, 147*, 103731.

[16] Harris, C. M., & Piersol, A. G. (2002). *Harris' shock and vibration handbook* (Vol. 5). New York: McGraw-Hill.

[17] Yang, T. H., Lee, Y. S., Yeon, K. W., Kim, H. M., Kim, J. Y., & Kwon, H. B. (2016). Estimation of the saw-tooth shock wave using a lead shock programmer. *Journal of Mechanical Science and Technology, 30*(5), 2133-2140.

[18] See http://www.donglingtech.com/en/cp3-2-14.htm, for more information about the pneumatic cylinder-type TWG.

[19] Neuburg, K. *A Study in the application of shock response, spectrum analysis to disk drive shipping and handling shock tests*. MSc Thesis, Faculty of the Department of Packaging Science, Rochester Institute of Technology, USA, 1995.

[20] Kallolimath, S., & Zhou, J. J. (2016). Optimal shock pulse in a drop test simulation of standardized board for uniform shock response. *Journal of Electronic Packaging, 138*(4), 1-10.

[21] Chin, I., Wong, S. F., & Chin, C. S. The very first Strain Range Bound Guidance methodology for system board shock evaluation. In *2010 34th IEEE/CPMT International Electronic Manufacturing Technology Symposium (IEMT)* (pp. 1-8). IEEE.

[22] Elfrink, R., Matova, S., De Nooijer, C., *et al*. (2011, December). Shock induced energy harvesting with a MEMS harvester for automotive applications. In *2011 International Electron Devices Meeting* (pp. 29.5.1-29.5.4). IEEE.

[23] Parzianello, G., Francesconi, A., & Pavarin, D. (2010). An estimation method for the Shock Response Spectrum propagating into plates subjected to hypervelocity impact. *Measurement, 43*(1), 92-102.

[24] Jin, Q. M. (1995). Mechanical simulation of shock test waveform. *Journal of Vibration and Shock, 14*(4), 46-51.

[25] Yao, H., Wen, J., Ren, Y., Wu, B., & Ji, Z. (2019, May). Low-cost measurement of industrial shock signals via deep learning calibration. In *2019 IEEE International Conference on Acoustics, Speech and Signal Processing (ICASSP)* (pp. 2892-2896). IEEE.

[26] Wen, J., Yao, H., Wu, B., Ren, Y., & Ji, Z. (2020). A deep learning approach to recover high-g shock signals from the faulty accelerometer. *IEEE Sensors Journal, 20*(4), 1761-1769.

[27] Li, Z., Abazari, A. M., Gerdroodbary, M. B., Manh, T. D., Nam, N. D., Valipour, P., ... & Babazadeh, H. (2020). Three-dimensional DSMC simulation of thermal Knudsen force in micro gas actuator for mass analysis of gas mixture. *Measurement, 160*, 107848.

[28] Dokainish, M. A., & Subbaraj, K. (1989). A survey of direct time-integration methods in computational structural dynamics—I. Explicit methods. *Computers & Structures, 32*(6), 1371-1386.

[29] Liu, G. R., & Quek, S. S. (2013). *The finite element method: a practical course*. Oxford, UK: Butterworth-Heinemann Elsevier.

[30] RAO, S. S., & YAP, F. F. (2014). *Mechanical vibrations*. Ed. 5. Upper Saddle River: Prentice Hall.

[31] Du Q., Sun Z., Huang C., & Zhai X. (2016). Impact dynamics modeling and simulation analyses of pneumatic cylinders. *China Mechanical Engineering, 27*(8), 1053-1058.

[32] Akhondizadeh, M. (2018). Analytical solution of the longitudinal wave propagation due to the single impact. *Journal of Low Frequency Noise, Vibration and Active Control, 37*(4), 849-858.

[33] Tribst J. P. M., de Morais D. C., Alonso A. A., Piva A. M. O. D., & Borges A. L. S. (2017). Comparative three-dimensional finite element analysis of implant-supported fixed complete arch mandibular prostheses in two materials. *Journal of Indian Prosthodontic Society, 17*(3), 255-260.

[34] http://www.chinaymc.com/product/showproduct.php?id=57&lang=en

[35] http://en.donglingtech.com/en/cp3-2.htm

CRediT authorship contribution statement

Jingjing Wen: Conceptualization, Funding acquisition, Investigation, Methodology, Visualization, Writing-original draft. **Houpu Yao:** Formal analysis, Writing-review & editing. **Bin Wu:** Resources, Supervision. **Ze Ji:** Software, Writing-review & editing. **Lihua Wen:** Project administration. **Man Xu** and **Yi Jin:** Software, Validation. **Xunliang Yan:** Resources, Funding acquisition, Supervision.

Highlights:

- Over deviation of the residual wave in trapezoidal shock pulse is investigated.
- The over deviation is diagnosed as the impact between the piston and the end cover.
- A 1D-continuous rod model is established to describe the impact behavior.
- Several modifications are proposed to alleviate the over deviation.
- A new separate-style TWG is designed based on the proposed modifications.

Declaration of Interest Statement

The authors declare that there is no conflict of interest.